Observations of the vertical distributions of summertime atmospheric pollutants in Nam Co: OH production and source analysis

Chengzhi Xing[1], Cheng Liu[2,1,3,5,*], Chunxiang Ye[4,*], Xiangguang Ji[7], Jingkai Xue[6], Jinping Ou[1], Hongyu Wu[6], and Qihou Hu[1]

[1] Key Lab of Environmental Optics & Technology, Anhui Institute of Optics and Fine Mechanics, Hefei Institutes of Physical Science, Chinese Academy of Sciences, Hefei, 230031, China

[2] Department of Precision Machinery and Precision Instrumentation, University of Science and Technology of China, Hefei, 230026, China

[3] Center for Excellence in Regional Atmospheric Environment, Institute of Urban Environment, Chinese Academy of Sciences, Xiamen, 361021, China

[4] College of Environmental Sciences and Engineering, Peking University, 100871 Beijing

[5] Key Laboratory of Precision Scientific Instrumentation of Anhui Higher Education Institutes, University of Science and Technology of China, Hefei, 230026, China

[6] School of Environmental Science and Optoelectronic Technology, University of Science and Technology of China, Hefei, 230026, China

[7] Institute of Physical Science and Information Technology, Anhui University, Hefei, 230601, China

*Corresponding author. E-mail: chliu81@ustc.edu.cn; c.ye@pku.edu.cn

1 **Abstract**

2 The Tibetan Plateau (TP) plays a key role in regional environment and global climate change, however,
3 the lack of vertical observation hinders a deeper understanding of the atmospheric chemistry and
4 atmospheric oxidation capacity (AOC) on the TP. In this study, we conducted MAX-DOAS
5 measurements at Nam Co, central TP, to observe the vertical profiles of aerosol, water vapor, NO_2,
6 HONO and O_3 from May to July 2019. In addition to NO_2 mainly exhibiting a Gaussian shape with the
7 maximum value appearing at 300-400 m, other four species all showed an exponential shape and
8 decreased with the increase of height. The maximum values of monthly averaged aerosol (0.17 km^{-1})
9 and O_3 (66.71 ppb) occurred on May, water vapor (3.68×10^{17} molec cm^{-3}) and HONO (0.13 ppb)
10 appeared on July, while NO_2 (0.39 ppb) occurred on June at 200-400 m layer. Water vapor, HONO and
11 O_3 all exhibited a multi-peak pattern, and aerosol appeared a bi-peak pattern for their averaged diurnal
12 variation. Moreover, we found O_3 and HONO were the main contributors to OH on the TP. The
13 averaged vertical profiles of OH production rates from O_3 and HONO all exhibited an exponential
14 shape, and decreased with the increase of height with the maximum values of 2.61 ppb/h and 0.49
15 ppb/h at the bottom layer, respectively. In addition, source analysis for HONO and O_3 were conducted
16 based on vertical observations. The heterogeneous reaction of NO_2 on wet surfaces was a significant
17 source of HONO, which obviously associated with water vapor concentration and aerosol extinction.
18 The maximum values of HONO/NO_2 appeared around water vapor being 1.0×10^{17} molec cm^{-3} and
19 aerosol being lager 0.15 km^{-1} under 1.0 km, and the maximum values usually accompanied with water
20 vapor being 1.0-2.0×10^{17} molec cm^{-3} and aerosol being lager 0.02 km^{-1} at 1.0-2.0 km. O_3 was
21 potentially sourced from south Asian subcontinent and Himalayas through long-range transport. Our
22 results enrich the new understanding of vertical distribution of atmospheric components and explained
23 the strong AOC on the TP.

24

25 **1 Introduction**

26 The Tibetan Plateau (TP) spans 2.5 million square kilometers with an average altitude of over 4000 m.
27 Therefore, the TP is called the "Third Pole" of the earth (Ma et al., 2020; Kang et al., 2022). It is the
28 home to tens of thousands of glaciers and nourishes more than 10 of Asia's rivers, thus it also acts the

29 role of "Water Tower of Asia" (Qu et al., 2019; Ma et al., 2022). Due to its special topography, the TP
30 is the heat source of atmosphere due the strong solar radiation, which as the driven force to profoundly
31 affect the regional atmospheric circulation, global weather conditions and climate change (Yanai et al.,
32 1992; Boos et al., 2010; Chen et al., 2015; Liu et al., 2022; Zhou et al., 2022). Monsoon rainfall in Asia,
33 flood over the Yangtze River valley, and El Niño in the Pacific Ocean are strongly associated with the
34 TP (Hsu et al., 2003; Li et al., 2016; Lei et al., 2019). In addition, the cyclone circulations caused by
35 the TP heat source also can inhibit the diffusion of atmospheric pollutants in the areas around the TP,
36 such as the Sichuan Basin, causing regional pollution (Zhang et al., 2019). Therefore, to improve
37 knowledge of the spatiotemporal evolutions and sources of atmospheric pollutants on the TP is of great
38 meaning and importance.

39 However, deciphering the atmospheric environment of the TP is highly challenging and dangerous, due
40 to its complex topography and harsh environment (Barnett et al., 2005; Bolch et al., 2012; Cong et al.,
41 2015; Kang et al., 2016). In order to unveil the feature of atmospheric composition over the TP and
42 their corresponding climate feedback, a large number of field observation stations have been
43 established, and a series of field campaigns have continued to be carried out recently, especially after
44 the performance of "the Second Tibetan Plateau Scientific Expedition and Research Program" (Che and
45 Zhao 2021; Wang et al., 2021; Ran et al., 2022). The China National Environmental Monitoring Center
46 (CNEMC) has established an in-situ monitoring network with more than 12 stations over the TP, such
47 as Lhasa, Shigatse, Shannan, Nyingchi, Nagqu, Ngari, Qamdo, Diqing, Aba, Guoluo, Xining, and
48 Haixi, to continuously monitor the surface concentrations of six atmospheric components (i.e. PM_{10},
49 $PM_{2.5}$, NO_2, SO_2, O_3 and CO) since 2013 (Gao et al., 2020; Li et al., 2020; Sun et al., 2021). The
50 Institute of Tibetan Plateau Research, Chinese Academy of Sciences, has also established six long-term
51 field observation stations to measure meteorological parameters and small amounts of atmospheric
52 composition (i.e. black carbon, aerosol optical density (AOD)) (Ma et al., 2020). In addition, scientists
53 are relying on advancements in satellite remote sensing technology, such as TROPOMI, OMI, MODIS
54 and CALIPSO, to monitor the spatial and temporal evolutions of atmospheric composition on the TP
55 (Zhu et al., 2019; Li et al., 2020; Rawat and Naja 2022). Their advantage is to obtain the column
56 densities of pollutants in a large-scale space of the TP. Although CALIPSO could detect aerosol
57 vertical profiles, the spatiotemporal resolution (i.e. ~5.0 km horizontal resolution, 0.06 km vertical
58 resolution and ~16 d temporal resolution) is limited and the data uncertainty in the planetary boundary
59 layer (PBL) is large due to the low signal-to-noise ratio (Huang et al., 2007). However, several studies
60 also revealed that the formation, aging and transport processes of atmospheric composition on the TP
61 occurs not only near the ground surface but also at high altitudes (Xu et al., 2020; Xu et al., 2022). The
62 high PBL on the TP caused by its strong solar radiation and undulating terrain promotes the
63 atmospheric exchange between the bottom troposphere and stratosphere (Yang et al., 2003; Seidel et al.,
64 2010). Therefore, the lack of vertical profiles of hinders the understanding of the evolution of trace
65 gases and their environmental and climate effects over the TP. In recent years, balloon and lidar
66 vertical measurements on the TP are occasionally carried out (Fang et al., 2019; Zhang et al., 2020;
67 Dong et al., 2022), but their limited detection species (i.e. aerosol and O_3) and high cost are obstacles
68 that limit long-term continuous observation and the conduction of more in-depth scientific research.
69 Multi-axis differential optical absorption spectroscopy (MAX-DOAS) has the technical advantage of
70 low-cost continuous observation of multiple atmospheric components (i.e. aerosol, O_3 and their
71 precursors) (Xing et al., 2017, 2019, 2020, 2021; Wang et al., 2018). Combining these data with better
72 scientific models can reduce the modeling bias and promote to better understand the physical, chemical
73 and dynamical processes.

74 The strong convergent airflow formed under the combined action of monsoon, subtropical anticyclone
75 and the airflow of subtropical westerlies could promote the accumulation of O_3 on the TP in summer
76 (Ye and Gao 1997). Therefore, several studies have revealed the high O_3 concentration on the TP (Li et
77 al., 2022; Yang et al., 2022; Yu et al., 2022). The strong solar radiation, high O_3 concentration and
78 relatively high humidity on the TP provide great potential for high OH production. Lin et al. (2008) and
79 Ye (2019) also confirmed that the high OH over the TP is mainly related to the reaction between $O(^1D)$
80 and water vapor. The $O(^1D)$ is produced from the photolysis of O_3 by UV radiation. Therefore, a

81 hypothesis of "strong atmospheric oxidation capacity (AOC) over the TP" was put forward. Previous
82 studies pointed out that nitrous acid (HONO) also play an important role in AOC at low-altitude areas,
83 and its contribution to OH can reach 40-60%, and even more than 80% in the early morning (Michoud
84 et al., 2012; Ryan et al., 2018; Xue et al., 2020). However, few HONO studies on the TP have been
85 reported. Our previous study operated at QOMS-CAS revealed that the HONO mainly distributed in
86 the lower PBL and peaked in summer with 1.11 ppb, which is comparable to the average level of
87 HONO in other low-altitude areas (Luo et al., 2010; Xing et al., 2021a, 2021b; Yang et al., 2021). It
88 indicates that it is also necessary to study the contribution of HONO to AOC on the TP. Furthermore,
89 understanding the vertical distribution of OH is of great significance for learning about the atmospheric
90 chemical processes and the evolution of atmospheric components on the TP (Zhou et al., 2015).
91 Identifying the sources of O_3 and HONO is the basis for studying the AOC on the TP. The limited
92 researches concluded that the atmospheric HONO on the TP is mainly sourced from the emissions of
93 vehicles, biomass burning and soil, except for the NO_2 heterogeneous reaction on aerosol surfaces
94 (Xing et al., 2021). The lower tropospheric O_3 on the TP is mainly dominated by local photochemical
95 reactions, regional horizontal transport, vertical mixing and the intrusion from stratosphere (Yin et al.,
96 2017; Xu et al. 2018).

97 In this study, we firstly analyzed the temporal and vertical characteristics of several atmospheric
98 components (i.e. aerosol, H_2O, NO_2, HONO and O_3) based on MAX-DOAS observations in Nam Co.
99 Afterwards, the contributions of O_3 and HONO to OH in the vertical space were discussed through the
100 TUV radiative transfer model and MAX-DOAS measurements. Finally, the potential sources of O_3 and
101 HONO at different altitudes were analyzed based on the MAX-DOAS retrievals.

2 Method and methodology

2.1 Measurement site

104 The Nam Co Monitoring and Research Station for Multisphere Interactions, CAS (NAMORS)
105 (30.774°N, 90.988°E; 4730 m a.s.l.) is located at the southeast banks of Nam Co lake and the foothills
106 of the northern Mt. Nyainqêntanglha (Fig. 1). The station land is covered by alpine meadows with soil
107 type of sandy silt loam. The southwest monsoon can carry abundant moisture from Indian Ocean to this
108 station in summer to increase humidity and precipitation there. Moreover, due to the summertime huge
109 evaporation from Nam Co lake, the atmospheric water vapour around CAS (NAMORS) is more
110 abundant than in other areas of the TP, resulting in lush grass vegetation and making the area around
111 this station an important summertime pasture. In addition, there are not large industries and cities
112 within 100 km of the CAS (NAMORS). The closest town to CAS (NAMORS) is Dangxiong county
113 which is about 60 km away from this station and lower about 500 m than this station. Only a small
114 number of vehicles pass through this area during summer tourism season. Therefore, no obvious
115 anthropogenic sources of air pollutants exist near this station. Averaged spatial distributions of aerosol
116 optical depth (AOD), O_3, NO_2 and HCHO monitored by satellite from May to July 2019 are shown in
117 Fig. S1. Elevated AOD, O_3, NO_2, and HCHO are mainly distributed in South Asian subcontinent (e.g.
118 India and Nepal), the southern foothills of the Himalayas, which is located in the upwind direction of
119 the southwest monsoon potentially affecting the atmospheric composition over CAS (NAMORS).
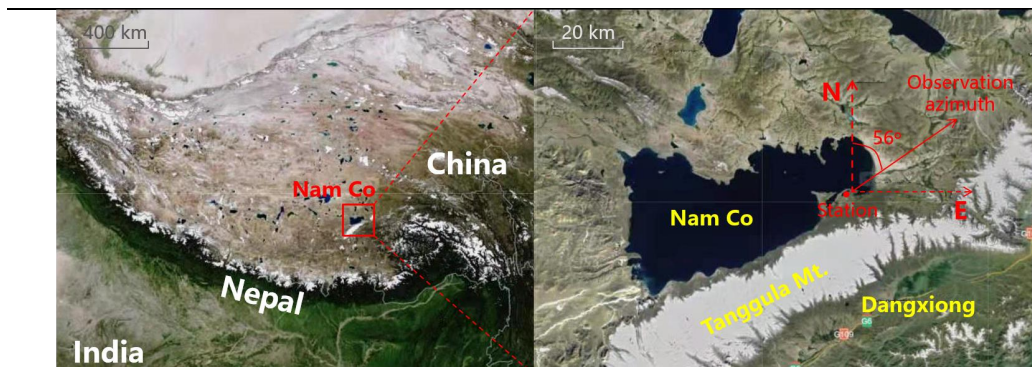
120

121 Figure 1. Geographical location of CAS (NAMORS) on the Tibet plateau.

122 **2.2 Instrument setup and data processing**

123 The MAX-DOAS instrument installed at CAS (NAMORS) was operated from 01 May to 09 July 2019.
124 It consists of three major parts: telescope unit, spectrometer unit and control unit. The detailed
125 description of this instrument can be found in Xing et al. (2021). In this study, the elevation angle
126 sequence was set to 1, 2, 3, 4, 5, 6, 8, 10,15, 30, and 90° with an exposure time of 60 s to each
127 individual spectrum. The azimuth angle was set to 56° pointing to Nagqu direction. Moreover, only
128 spectra collected under solar zenith angle (SZA) less than 75° was used for spectral analysis to avoid
129 the strong stratospheric absorption.

130 The differential slant column densities (DSCDs) of the oxygen dimer (O_4), water vapor (H_2O), NO_2,
131 HONO and O_3 were retrieved using QDOAS software (http://uvvis.aeronomie.be/software/QDOAS/)
132 developed by Royal Belgian Institute for Space Aeronomy (BIRA-IASB). The zenith spectrum
133 measured at every sequence were selected as scan Frauenhofer reference spectrum. The retrieval
134 configurations of O_4, H_2O, NO_2, HONO and O_3 followed Xing et al. (2017), Lin et al. (2020), Xing et
135 al. (2021), Wang et al. (2020) and Wang et al. (2018), respectively. The detailed DOAS fit settings of
136 above five species were listed in Table 1. Corrected I_0 (Aliwell et al., 2002) was used in this study. Fig.
137 2 shows a typical DOAS retrieval example for above five species. DOAS fit results with root mean
138 square (RMS) values larger than 5×10^{-4}, 5×10^{-4}, 5×10^{-4}, 1×10^{-3}, and 6×10^{-4} for O_4, H_2O, NO_2,
139 HONO, and O_3, respectively, were filtered out. In addition, we calculated color index (CI) to remove
140 cloud effect (Wagner et al., 2016). The data filter criteria according to CI followed by Ryan et al. (2018)
141 and Xing et al. (2020). Afterwards, the quantified DSCDs of O_4, H_2O, NO_2, HONO, and O_3 remained
142 91.33%, 91.97%, 92.16%, 86.42% and 81.09%, respectively.

143 The vertical profiles of aerosol and trace gases (i.e. H_2O, NO_2, HONO and O_3) were retrieved using
144 algorithm based on optimal estimation method (OEM). A linearized pseudo-spherical vector discrete
145 ordinate radiative transfer model VLIDORT was used as forward model and a Gauss-Newton (GN)
146 scheme was used as the inversion strategy (Wedderburn et al., 1974). The detailed description of this
147 algorithm can be found in Liu et al. (2021), Xing et al. (2021) and Wang et al. (2018). In this study, the
148 initial a priori profile shape of above five species was set to exponential decreasing shape, and the
149 AOD and VCDs simulated by WRF-Chem were also used as initial input a priori information to
150 constrain the retrieval process. For the O_3 profile retrieval, the stratospheric O_3 profile was deducted
151 using TROPOMI O_3 profile (Zhao et al., 2021). We set 20 vertical layers from 0.0 to 4.0 km with a
152 vertical resolution of 0.2 km. The correlation height was set to 1.0 km. Moreover, the surface albedo,
153 single scattering albedo and asymmetry parameter were set to fixed constant of 0.08, 0.85 and 0.65,
154 respectively (Irie et al., 2008). The retrieved vertical profiles were removed under the condition of
155 degree of freedom (DOF) and relative error less than 1.0 and 100%, respectively.

156 **Table 1.** Detailed DOAS retrieval settings for O_4, H_2O, NO_2, HONO and O_3.

Parameter	Data source	Fitting intervals (nm)				
		O_4	H_2O	NO_2	HONO	O_3

Wavelength range		338-370	433-455	338-370	340-373	320-340
NO_2	298K, I_0-corrected, Vandaele et al. (1998)	✓	✓	✓	✓	✓
NO_2	220K, I_0-corrected, Vandaele et al. (1998)	✓	✓	✓	✓	✗
O_3	223K, I_0-corrected, Serdyuchenko et al. (2014)	✓	✓	✓	✓	✓
O_3	243K, I_0-corrected, Serdyuchenko et al. (2014)	✓	✗	✓	✓	✗
O_3	293K, I_0-corrected, Serdyuchenko et al. (2014)	✗	✗	✗	✗	✓
O_4	293K, Thalman and Volkamer (2013)	✓	✓	✓	✓	✓
HCHO	298K, Meller and Moortgat (2000)	✓	✗	✓	✓	✓
Glyoxal	298K, Volkamer (2005)	✗	✓	✗	✗	✗
H_2O	HITEMP (Rothman et al. 2010)	✓	✓	✓	✓	✗
BrO	223K, Fleischmann et al. (2004)	✓	✗	✓	✓	✗
HONO	296K, Stutz et al. (2000)	✗	✗	✗	✓	✗
Ring	Calculated with QDOAS	✓	✓	✓	✓	✓
Polynomial degree		Order 3	Order 3	Order 3	Order 5	Order 3
Intensity offset		Constant	Constant	Constant	Constant	No

157

158
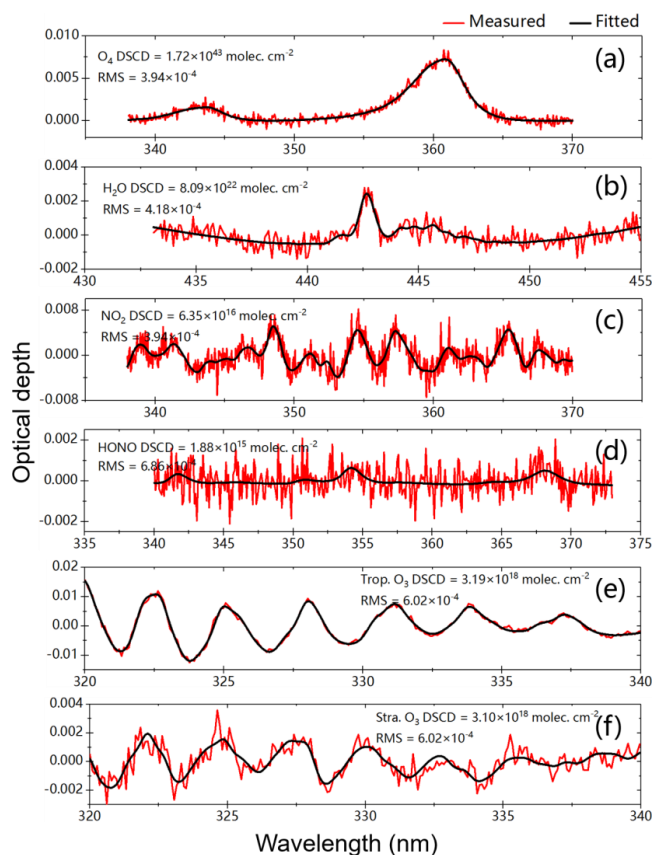
Figure 2. DOAS fit examples of O_4, H_2O, NO_2, HCHO, tropospheric O_3 and stratospheric O_3. The red
line and black line represent the measured and fitted results, respectively.

2.3 TUV model

The calculation of photolysis rates of HONO and O_3 used tropospheric ultraviolet and visible (TUV) radiation model (https://www2.acom.ucar.edu/modeling/tropospheric-ultraviolet-and-visible-tuv-radiation-model) based on a full FORTRAN code, and this model usually runs accurately in clean, sunny and cloudless days. The initial input parameters were as follows: the aerosol optical depth (AOD) at 361 nm was derived from aerosol extinction profiles measured by MAX-DOAS; the daily total ozone column density was measured by TROPOMI with a value range of 260-280 DU; the single scattering albedo (SSA) was calculated based on the regression analysis of multi-wavelength (361 and 477 nm) O_4 absorptions measured by MAX-DOAS (Xing et al., 2019); fixed Ångström exponents of 0.508, 0.581 and 0.713 were used in May, June and July, respectively, referring to Xia et al. (2011).

2.4 Backward trajectory, PSCF and CWT analysis

The 48-h backward trajectories at five heights of 200, 600, 1000, 1400 and 1800 m were calculated using the Hybrid Single-particle Lagrangian Integrated Trajectory (HYSPLIT) model based on the Global Data Assimilation System (GDAS) to identify the major transport pathways of O_3 (Draxler and Hess, 1998). Moreover, the calculated backward trajectories were clustered into three groups using Ward's variance method and Angle Distance algorithm.

In order to determine the potential source locations of O_3 over CAS (NAMORS), the Potential Source Contribution Function (PSCF) model and Concentration Weighted Trajectory (CWT) model were used (Hong et al., 2019; Ou et al., 2021). The PSCF was calculated through the number of air trajectory endpoints being divided by the number of air trajectory endpoints. Moreover, a weighting function was introduced to reduce the increased uncertainties of PSCF with the increase of the distance between the grid and sampling point. In this study, the set of this weighting function referred to Yin et al. (2017). CWT can be used to calculate the weight concentration through averaging the concentrations associated with trajectories crossing the grid cell. Above weighting function was also introduced to calculate the WCWT (Hsu, et al., 2003). The detailed description of these two models can be found in Wang et al., 2006.

2.5 Ancillary data

The surface NO_2, HONO and O_3 concentrations used to validate the corresponding MAX-DOAS measurements were monitored by broadband cavity enhanced spectrometer (BBCES) (Fang et al., 2017), long path absorption photometer (LOPAP) (Kleffmann et al., 2008) and Thermo Electron 49i (Shi et al., 2009), respectively. The planetary boundary layer height (PBLH) was simulated using Weather Research and Forecasting model (WRF) with spatiotemporal resolutions of 20×20 km^2 and 1.0 hour (detailed configurations in Appendix). Moreover, the large-scaled spatial distributions of AOD, O_3, NO_2 and HCHO over CAS (NAMORS) were monitored by Himawari-8 (Bessho et al., 2016), Ozone Monitoring Instrument (OMI) (Veefkind et al., 2004) and Tropospheric Monitoring Instrument (TROPOMI) (Griffin et al., 2018; Su et al., 2020), respectively.

3 Results

3.1 Overview of the measurements

Figure 3 showed the averaged diurnal variation of AOD from 1st May to 9th July 2019, with an average value of 0.076 km^{-1} during 08:00-19:00. The AOD was 0.071 km^{-1} at 08:00, and then gradually decreased to a minimum value of 0.052 km^{-1} at 12:00. Subsequently, the AOD increases significantly, reaching maximum values during 15:00-17:00 (average of 0.107km^{-1}), which was about 1.408 times the diurnal average value. Such an enhancement of AOD may be related to the long-range transport of aerosol from southern Asia (Yang et al., 2020; Bi et al., 2023). Moreover, 15:00-17:00 was the active time of tourists and local residents (i.e. cooking), and these kinds of anthropogenic sources contributed to the atmospheric AOD of NAMORS through short-distance transport (Yin et al., 2017; Zhang et al., 2017). After 17:00, the AODs decreased rapidly to 0.071 km^{-1} at 18:00 and 0.081 km^{-1} at 19:00, respectively.
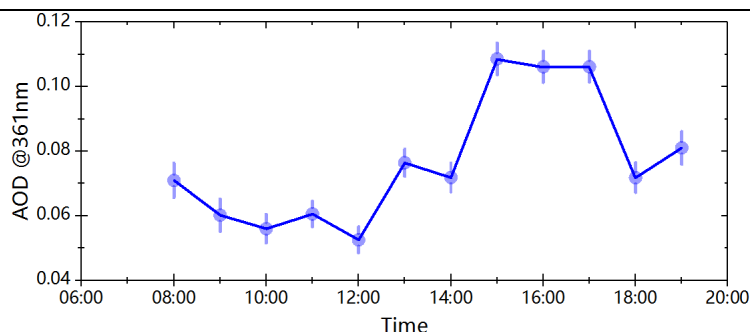
Figure 3. Averaged diurnal variation of AOD at CAS (NAMORS).

As shown in Figure S2, the diurnal variation of PBL in Nam Co from May to July 2019 shown lower in the early morning and late afternoon, and higher between 11:00 and 17:00 with the maximum PBL larger than 2.0 km. Zhang et al. (2017) and Yang et al., (2017) also reported that the PBL in Nam Co was usually larger than 1.0 km during daytime in spring and summer. Five typical height layers under the PBL (0.0-0.2 km, 0.4-0.6 km, 0.8-1.0 km, 1.2-1.4 km and 1.6-1.8 km) were thus selected to investigate the height-dependent variations of aerosol, H_2O, NO_2, HONO and O_3 during the observations.

Figure 4 showed the time series of the daily averaged aerosol, H_2O, NO_2, HONO and O_3 at above five layers from 1st May to 9th July 2019. Aerosol mainly distributed at 0.0-0.2 km with an average extinction coefficient of 0.138 km^{-1}, and the ratios of aerosol extinction at 0.4-0.6 km, 0.8-1.0 km, 1.2-1.4 km and 1.6-1.8 km to those at 0.0-0.2 km were 39.34%, 18.77%, 7.29% and 2.62%, respectively. That indicated that the aerosol was usually local-emitted at the surface, and the occasionally appearance of strong aerosol extinction at 0.4-0.6 km, such as 13th and 30th June, was associated with long-range transport from south Asia (Wan et al., 2015; Li et al., 2016). The average concentration of H_2O at 0.0-0.2 km was 2.35×10^{17} molec cm^{-3}, and the ratios of H_2O at 0.4-0.6 km, 0.8-1.0 km, 1.2-1.4 km and 1.6-1.8 km to those at 0.0-0.2 km were 83.40%, 68.08%, 50.64% and 35.74%, respectively, which should attribute to the transport of H_2O from Indian Ocean during the monsoon and the elevated evaporation from Nam Co lake to lead to its not obvious vertical gradient (Lei et al., 2014; Zhu et al., 2019). The average concentration of NO_2 at 0.0-0.2 km was 0.193 ppb, and its high concentration mainly distributed at 0.4-0.6 km after 15th May. The ratios of NO_2 at 0.4-0.6 km, 0.8-1.0 km, 1.2-1.4 km and 1.6-1.8 km to those at the bottom layer were 104.03%, 59.05%, 24.62% and 12.84%, respectively. The elevation of the distribution height of high concentration NO_2 should be attributed to the transport process from the NO_x produced by ice and snow on the top of Mt. Tanggula under strong ultraviolet radiation (Boxe et al., 2005). As depicted in Figure S3, the WPSCF passing through Mt. Tanggula showed high values at 300-400 m layer, especially at 400 m (> 0.3). HONO mainly distributed at 0.0-0.2 km with an average value of 0.087 ppb, and the ratios of HONO at 0.4-0.6 km, 0.8-1.0 km, 1.2-1.4 km and 1.6-1.8 km to those at 0.0-0.2 km were 58.49%, 44.64%, 31.30% and 21.67%, respectively. That indicated that the primary and secondary sources of HONO were mainly at the surface (Section 4.2). The vertical gradient of O_3 concentration was also not obvious, which was associated with its vertical mixing and photochemical production (Yin et al., 2017). As shown in Figure S4, the corresponding TROPOMI O_3 profiles around Nam Co and several lidar and ozonesonde measured O_3 profiles on the TP in several previous studies also exhibited an exponential shape (Fang et al., 2019; Zhang et al., 2020; Yu et al., 2022). The O_3 average concentration at 0.0-0.2 km was 63.030 ppb, and the ratios of O_3 at 0.4-0.6 km, 0.8-1.0 km, 1.2-1.4 km and 1.6-1.8 km to those at surface were 89.25%, 82.44%, 80.16% and 79.13%, respectively.
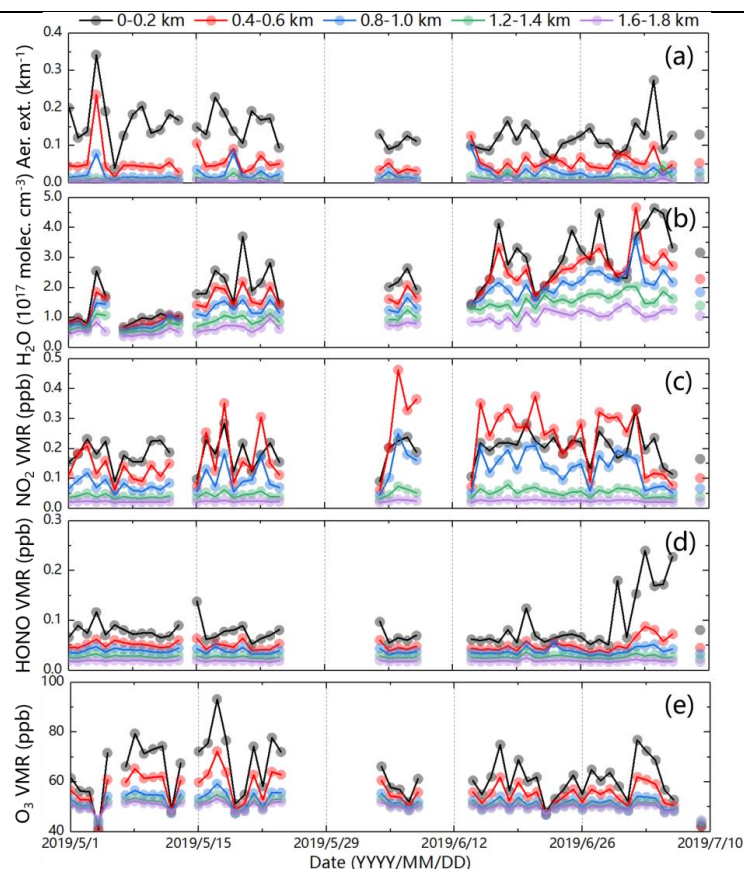
248 Figure 4. Time series of (a) aerosol extinction, (b) Water vapour, (c) NO₂, (d) HONO, and (e) O₃
249 monitored by MAX-DOAS at 0-0.2, 0.4-0.6, 0.8-1.0, 1.2-1.4 and 1.6-1.8 km five height layers from 01
250 May to 09 July 2019.

3.2 Vertical distributions of aerosol, H₂O, NO₂ and HONO

252 The first row in Figure 5 provided the averaged vertical profiles of aerosol, H_2O, NO_2, HONO and O_3
253 from May to July 2019. We found that the vertical profiles of aerosol, H_2O, HONO and O_3 all
254 exhibited an exponential shape with maximum values near the surface, while NO_2 exhibited a Gaussian
255 shape with the maximum value of 0.321 ppb occurring at 0.3-0.4 km layer. In addition to the effect of
256 NO_x transport, Xu et al. (2018) also revealed that the long-range high-altitude transport process from
257 the northern south Asian subcontinent can significantly enhance the Nam Co's peroxyacetyl nitrate
258 (PAN) level which is a reservoir of NO_x. As shown in the second row of Figure 5, the monthly
259 averaged aerosol vertical profiles from May to July 2019 all exhibited an exponential shape, and varied
260 in the order of May (0.17 km^{-1}) > July (0.14 km^{-1}) > June (0.11 km^{-1}). Xu et al. (2018) and Neupane et
261 al. (2019) also reported a similar monthly variations of black carbon (BC) from May to July over the
262 TP, and revealed that it was mainly associated with the anthropogenic emissions (i.e. biomass burning)
263 and its transport from south Asia. The monthly averaged vertical profile of H_2O in May and July
264 exhibited an exponential shape, while its maximum concentration layer slightly elevated to 0.1-0.2 km
265 which was related to the strongest monsoon transport (Xu et al., 2020). It varied in the order of July
266 (3.68×10^{17} molec cm^{-3}) > June (2.71×10^{17} molec cm^{-3}) > May (2.26×10^{17} molec cm^{-3}), and its
267 maximum concentration occurring in July was strongly associated with the enhanced evaporation from
268 the Nam Co lake (Xu et al., 2011). The monthly averaged vertical profiles of NO_2 all exhibited a
269 Gaussian shape from May to July, and its maximum values mainly distributed at 0.2-0.4 km layer
270 varying in the order of June (0.39 ppb) > May (0.31 ppb) > July (0.28 ppb). It indicated that the

271 regional transport from the NO_x produced from ice and snow under strong shortwave radiation (Figure
272 S3), NO_2 emitted from vehicles due to the increased tourism, anthropogenic emissions from local
273 residents (i.e. biomass burning and religious activities) played an important role in the vertical
274 distribution characteristic of NO_2 (Boxe et al., 2005; Chen et al., 2019). The monthly averaged vertical
275 profiles of HONO from May to July all exhibited an exponential shape, with maximum values near the
276 surface varying in the order of July (0.13 ppb) > May (0.07 ppb) > June (0.06 ppb). The local direct
277 emissions from biomass burning, vehicles and soil should be main sources of the surface HONO (Xing
278 et al., 2021). Moreover, the heterogeneous reaction of NO_2 on wet surfaces should be another important
279 source of HONO at different height layers (Section 4.2). For example, the aerosol extinction coefficient,
280 and the concentrations of H_2O and NO_2 were all relatively large at the bottom layer in July,
281 correspondingly, we observed the highest concentration of HONO near the surface in this month. The
282 monthly averaged O_3 vertical profiles all showed an exponential shape from May to July, and its
283 surface concentration varied in the order of May (66.71 ppb) > July (61.45 ppb) > June (59.55 ppb).
284 This kind of monthly variation trend of O_3 was also reported by several previous studies (Yin et al.,
285 2017; Xu et al., 2018). The O_3 in Nam Co was mainly sourced from stratospheric intrusion,
286 photochemical reactions, long-range transport and local vertical mixing (Yin et al., 2017; Chen et al.,
287 2019).
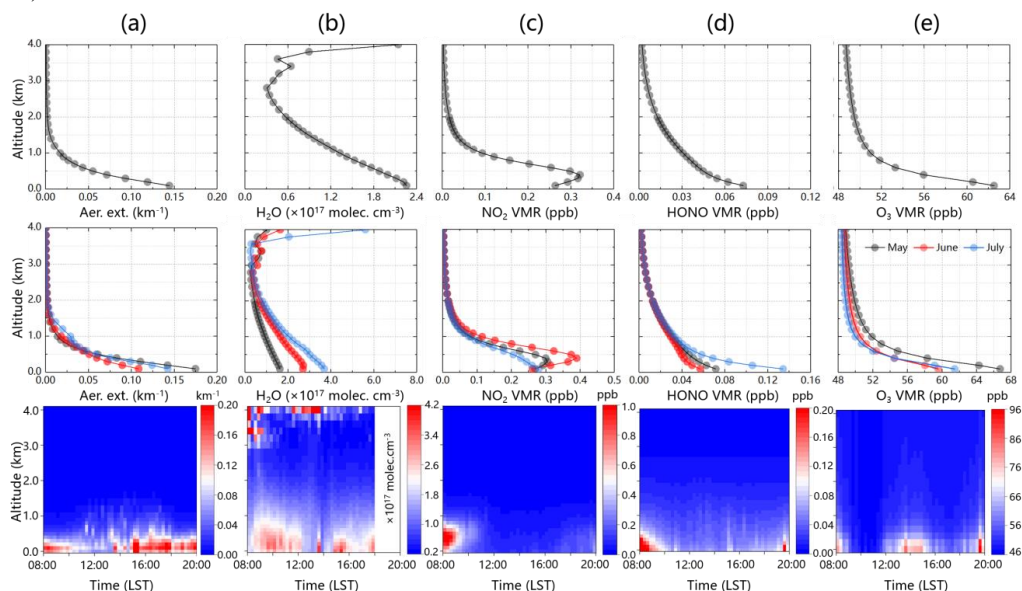
288

289 Figure 5. Vertical profiles of (a) aerosol extinction, (b) Water vapour, (c) NO_2, (d) HONO, and (e) O_3.
290 The top row shows the averaged vertical profiles from 01 May to 09 July 2019. The middle row shows
291 the monthly averaged vertical profiles. The bottom row shows the averaged diurnal vertical profiles
292 from 01 May to 09 July 2019.

293 The third row in Figure 5 illustrated the averaged diurnal variations in vertical profiles of aerosol, H_2O,
294 NO_2, HONO and O_3 from May to July 2019. Aerosol mainly distributed under 1.0 km, especially 0.6
295 km, and its mixing height was gradually increased with the rise of the PBL height after 12:00.
296 Moreover, the diurnal variation of aerosol showed a bi-peak pattern, which was in line with the
297 investigation reported by Pokharel et al. (2019). The first peak occurred between 08:00-10:00, and
298 another appeared after 15:00. This pattern was dominated by the local emission and regional transport
299 of aerosol (Zhang et al., 2017; Pokharel et al., 2019). Moreover, the interaction between local sandy silt
300 loam surface and local meteorology was another significant driving force with the wind speed less than
301 2.3 m/s and 4.0 m/s under 10 m and 500 m, respectively (Figure S5). H_2O mainly distributed under 1.0
302 km and above 3.0 km, and its diurnal variation exhibited a multi-peak pattern. The first peak appeared
303 between 08:00-12:00, which was mainly affected by the monsoon driven long-range transport of H_2O

304   (Cong et al., 2009; Xu et al., 2020). The second and third peaks occurred at 15:00-16:00 and after
305   17:00, respectively. In addition to long-range transport, the enhanced evaporation from the Nam Co
306   lake also significantly contributed to the appearance of these two peaks of H_2O (Xu et al., 2011). NO_2
307   mainly distributed at 0.2-0.4 km, and peaked before 10:00 and after 18:00 which were dominated by
308   the effects of local emissions and regional transport (Figure S3) (Boxe et al., 2005; Chen et al., 2019).
309   Moreover, its diurnal mixing height was obviously correlated to the diurnal evolution of PBL height.
310   HONO mainly distributed under 1.0 km, especially 0.4 km. Its diurnal variation showed a multi-peak
311   pattern with three obvious peaks before 10:00, 15:00-16:00, and after 19:00. In addition to local
312   emissions (i.e. vehicle emission, biomass burning and soil emission), the heterogeneous reaction of
313   NO_2 on wet surfaces should be also an important HONO source (Xing et al., 2021). We found that
314   there were larger aerosol extinction (> 0.12 km^{-1}) and higher concentrations of NO_2 (> 0.20 ppb) and
315   H_2O (> 2.27 molec cm^{-3}) around three HONO peaks. O_3 mainly distributed under 0.4 km, and its
316   diurnal variation exhibited a multi-peak pattern with three peaks appearing before 09:00, 13:00-15:00
317   and after 19:00. The appearance of O_3 peaks was mainly associated with the influence of the complex
318   topography of the TP, long-range transport, local vertical mixing and stratospheric intrusion (Yin et al.,
319   2017; Chen et al., 2019; Qian et al., 2022). The active photochemical reaction should be another
320   important source of O_3, especially for its second peak at 13:00-15:00.

3.3 Validation with independent data

322   In order to validate the MAX-DOAS dataset, we extracted the concentrations of NO_2, HONO and O_3 at
323   the bottom layer (0.0-0.1 km) from their corresponding vertical profiles to compare with in situ
324   measurements. As shown in Figure 6(a-c), we found good agreements between MAX-DOAS and in
325   situ observations with Pearson correlation coefficients (R) of 0.91, 0.62 and 0.82 (regression slope of
326   0.89, 1.05 and 0.82) for NO_2, HONO and O_3, respectively. That indicated the good reliability of trace
327   gases from MAX-DOAS retrievals. Moreover, we also compared the MAX-DOAS PBL and WRF PBL,
328   and a similar variation trend was found. However, WRF PBL showed a significantly difference in
329   height values with MAX-DOAS PBL before 12:00. That should be due to the simulation uncertainties
330   for WRF model at Tibetan plateau with complex topography and meteorology (Yang et al., 2016; Xu et
331   al., 2019).
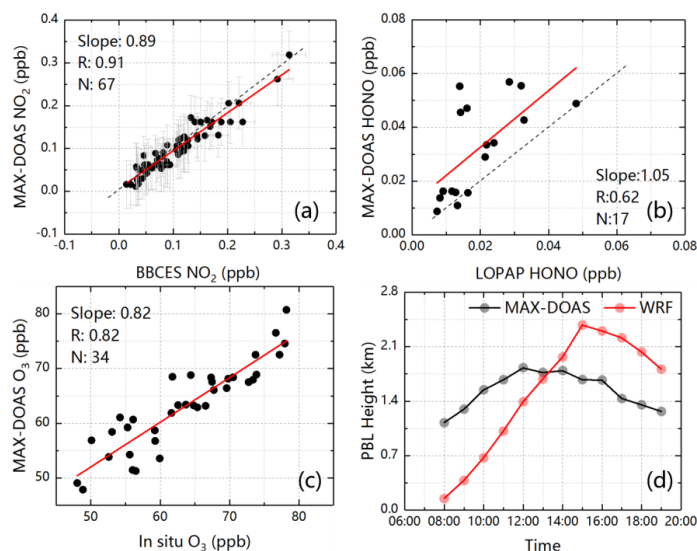
Figure 6. Validations of (a) MAX-DOAS NO_2 vs in situ NO_2, (b) MAX-DOAS HONO vs LOPAP
HONO, (c) MAX-DOAS O_3 vs in situ O_3, and (d) MAX-DOAS PBL vs WRF PBL.

4 Discussion

4.1 OH production

337 HONO and O_3 are two important precursors of OH redical to enhance the AOC (Kleffmann et al., 2005;
338 Ryan et al., 2018; Xing et al., 2021). In order to evaluate the AOC on the TP, we tried to analyze the
339 OH production from HONO and O_3 at different height layers through vertical observations and TUV
340 calculations. The OH production rates from HONO and O_3 were calculated using the following two
341 equations:

342 $$P\left(OH\right)_{HONO} = J\left(HONO\right) \times [HONO]$$

343 $$P\left(OH\right)_{O_3} = 2 \times f \times J\left(O\left(^1D\right)\right) \times [O_3]$$

344 Where $J(HONO)$ and $J(O(^1D))$ were the photolysis rates of HONO and $O(^1D)$ calculated using TUV
345 model. $O(^1D)$ was the product from O_3 photolysis by UV radiation. f was the fraction of the process
346 $O(^1D) + H_2O \rightarrow 2OH$.

347 Figure 7(a-b) showed the averaged diurnal vertical distributions of the photolysis rates $J(HONO)$ and
348 $J(O(^1D))$ from May to July 2019. We found that the maximum $J(HONO)$ and $J(O(^1D))$ were all
349 appeared at the bottom layer between 12:30 and 15:30 with values of 2.0×10^{-3} and 6.75×10^{-5} s^{-1},
350 respectively. The maximum values were usually larger than that at low-altitude areas due to the
351 stronger solar UV radiation on the TP (Su et al., 2008; Xing et al., 2021; Yang et al., 2021; Liu et al.,
352 2022), but being consistent with the values on the TP reported by Lin et al. (2008). Moreover, it should
353 be noted that the values of $J(HONO)$ and $J(O(^1D))$ all decreased with the increase of altitude, which
354 was significantly different with previous studies in low altitudes (Ryan et al., 2018; Xing et al., 2021;
355 Xu et al., 2021).
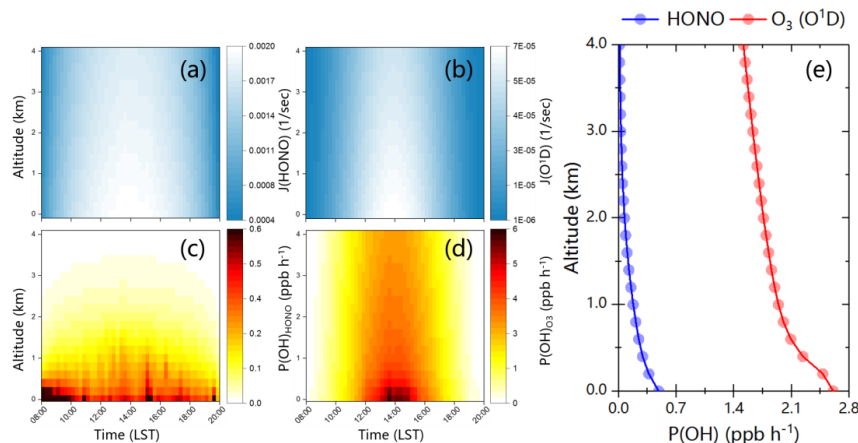
356

357 Figure 7. Averaged diurnal vertical profiles of the (a) photolysis rate $J(HONO)$, (b) photolysis rate
358 $J(O(^1D))$, (c) OH radical production rates from HONO photolysis, (d) OH radical production rates from
359 O_3 photolysis. (e) shows the averaged vertical profiles of OH radical production rates from HONO and
360 O_3 photolysis from 01 May to 09 July 2019.

361 Figure 7(c-d) showed the averaged diurnal vertical profiles of OH production rates from HONO and O_3
362 photolysis from May to July 2019. $P(OH)_{HONO}$ exhibited a multi-peak pattern which mainly appeared
363 before 10:00, 15:00-16:00, and after 19:00 at 0-0.4 km with a maximum value of 0.81 ppb/h. While
364 $P(OH)_{O_3}$ showed a unimodal pattern occurring at 13:00-15:00 under 0.4 km with a maximum value of
365 6.20 ppb/h. The averaged vertical profiles of $P(OH)_{HONO}$ and $P(OH)_{O_3}$ during the observation were
366 depicted in Figure 7(e). We found that the maximum values of $P(OH)_{HONO}$ (0.49 ppb/h) and $P(OH)_{O_3}$
367 (2.61 ppb/h) all appeared at the bottom layer, and decreased with height. That indicated O_3 was the
368 main contributor of OH production (> 80%) on the TP, which was about 5-6 times to HONO.
369 Moreover, the OH production rates from HONO and O_3 in other cities of China were depicted in Table
370 2. The contribution percentage of O_3 to P(OH) in Nam Co was significantly higher than that in other
371 cities, which was due to the relatively high concentrations of O_3 and H_2O, and the strong radiation in

372 Nam Co. In addition, P(OH)_HONO in Nam Co was close to that in relatively dry areas (i.e. Beijing and
373 Xianghe), but slightly lower than that in areas with relatively high humidity which can enhance the
374 heterogeneous production of HONO (Ryan et al., 2018; Liu et al., 2019; Xing et al., 2021).

375 Table 2. The maximum OH production rates contributed from HONO and O$_3$ at different locations.

Location	Date	$P(OH)_{HONO}$ (ppb/h)	$P(OH)_{O3}$ (ppb/h)	References
Xianghe (China)	Jul. 2008-Apr. 2009	~0.80 in Spring ~0.70 in Summer	~0.20 in Spring, ~0.45 in Summer	Hendrick et al. (2014)
Beijing (China)	Mar. 2010-Dec. 2012	~1.25 in Spring, ~0.70 in Summer	~0.10 in Spring, ~0.55 in Summer	Hendrick et al. (2014)
East China Sea (China)	Jun. 2017	~1.75	~1.20	Cui et al. (2019)
Chengdu (China)	Aug.-Sep. 2019	~3.25	-	Yang et al. (2021)
Qingdao (China)	Jul.-Aug. 2019	~1.30	~1.00	Yang et al. (2021)
Nam Co (China)	May-Jul. 2019	0.81	6.20	This study

4.2 Possible daytime HONO sources

377 Atmospheric HONO mainly sourced from direct emission, homogeneous reaction and heterogeneous
378 reaction (Fu et al., 2019; Ren et al., 2020; Chai et al., 2021; Crilley et al., 2021; Li et al., 2021). There
379 were less anthropogenic emissions for HONO around NAMORS, however, the open burning of crop
380 residues and soil emissions should be important HONO sources considering the pasture environment
381 and large amounts of animal manure (Cui et al., 2021a; 2021b). Moreover, the background of low-level
382 NO on the TP leaded to the homogeneous reaction not to be the main source of HONO at NAMORS
383 (Lin et al., 2019; Xing et al., 2021; Li et al., 2022). Heterogeneous reaction of NO$_2$ on wet surfaces
384 became an important potential source of HONO around NAMORS, which affected by the humidity,
385 temperature, solar radiation, aerosol concentration and corresponding specific surface area. In order to
386 remove the effect of diurnal PBL evolution, we used HONO/NO$_2$ to indicate the extent of the
387 heterogeneous reaction process. As shown in Figure 8, scatter plots between HONO/NO$_2$ and water
388 vapor were illustrated. We found that the maximum value of HONO/NO$_2$ appeared around water vapor
389 being around 1.0×10^{17} molec cm^{-3} under 1.0 km, and being around $1.0-2.0\times10^{17}$ molec cm^{-3} at
390 1.0-2.0 km height layer. This phenomenon of HONO/NO$_2$ first increasing and then decreasing with the
391 increasing of water vapor (or relative humidity) was usually found in low-altitude areas in previous
392 studies (Wang et al., 2013; Liu et al., 2019; Xing et al., 2021; Xu et al., 2021). When the water vapor
393 was greater than above mentioned critical values at different heights, HONO/NO$_2$ gradually decreased,
394 which was related to the efficient uptake of HONO and the decrease of NO$_2$ reactivity with the increase
395 of water vapor (Liu et al., 2019; Xu et al., 2021). That indicated water vapor has significant
396 enhancement for the conversion rate of NO$_2$ to HONO. Moreover, we found that the high value areas
397 of HONO/NO$_2$ at above five height layers were all accompanied by high aerosol extinction (> 0.15
398 km^{-1} under 1.0 km, and > 0.02 km^{-1} at 1.0-2.0 km). It indicated that aerosol surface has contribution to
399 the heterogeneous reaction process of NO$_2$. The scatter plots between HONO and NO$_2$ at above five
400 layers (Figure S6) also confirmed the possibility of the NO$_2$ heterogeneous reaction to generate HONO
401 on the TP, and the contribution of atmospheric water vapor and aerosol extinction to this process.

402
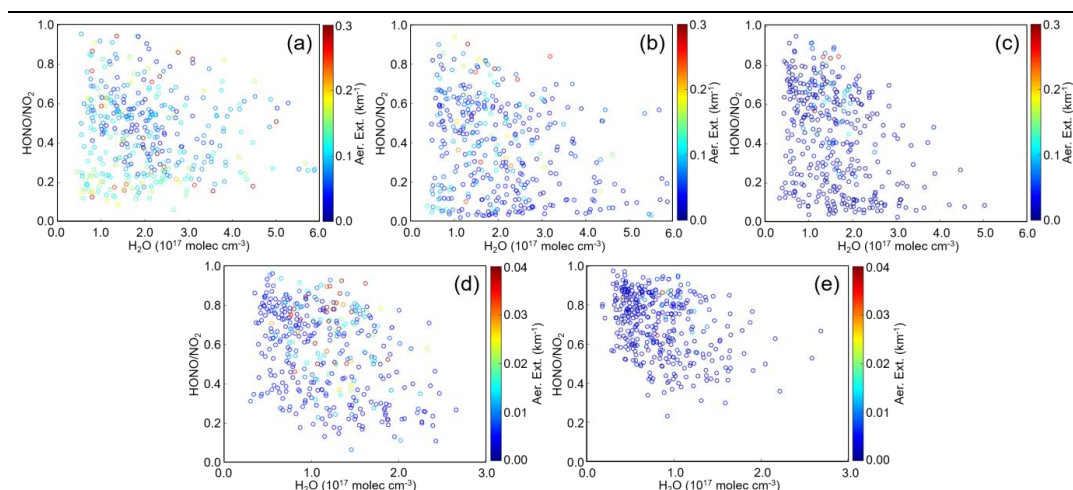
Figure 8. Scatter plots between HONO/NO$_2$ and water vapor coloured by aerosol extinction at (a)
0.0-0.2 km, (b) 0.4-0.6 km, (c) 0.8-1.0 km, (d) 1.2-1.4 km, (and e) 1.6-1.8 km from 1st May to 9th July
2019.

In Figure 9, the vertical profile of HONO/NO$_2$ from May to July 2019 was depicted. We found that
HONO/NO$_2$ firstly decreased and then increased with the increasing of height, which was opposite to
previous studies in low-altitude areas (Meng et al., 2020; Zhang et al., 2020; Xing et al., 2021; Xu et al.,
2021). The minimum average HONO/NO$_2$ occurred at 0.3-0.4 km height layer with a value of 0.37.
The relatively high values of HONO/NO$_2$ at the bottom layer should be related to the non-deducted
HONO direct emissions.

412
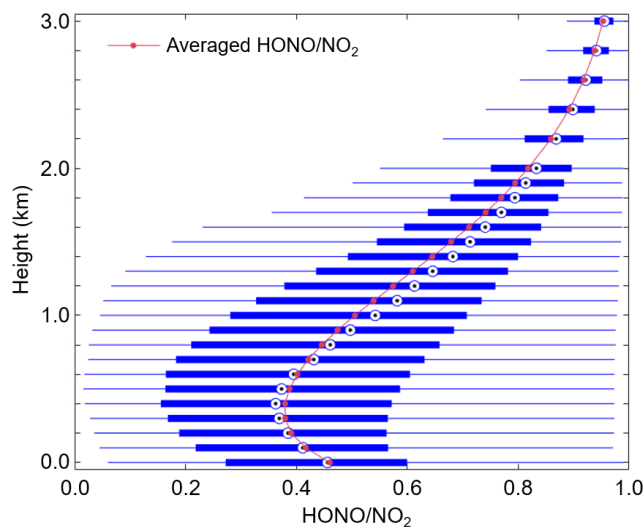
Figure 9. Vertical profile of HONO/NO$_2$ from 1st May to 9th July 2019.

4.3 Possible daytime O$_3$ sources

In addition to local photochemistry process, long-range transport was the main source of O$_3$ on the TP
(Yin et al., 2017; Xu et al., 2018). To further understand the transport pathway and potential source of
O$_3$, cluster analysis, WPSCF and WCWT models were used to assess the regional representativity of
O$_3$ at five typical heights (200 m, 600 m, 1000 m, 1400 m and 1800 m). As shown in Figure S7 and
Table 3, the backward trajectories arriving at NAMORS during the observation were classified into

420 three clusters. We found that cluster 3 was associated with the highest O_3 concentration at 200 m
421 (65.48 ± 17.41 ppb) and 1800 m (49.69 ± 2.21 ppb), and cluster 1 were related to the highest O_3
422 concentration at 600 m (54.67 ± 6.94 ppb), 1000 m (51.61 ± 3.84 ppb) and 1400 m (50.51 ± 2.89 ppb).
423 These two clusters were all originating from northwestern of south Asian subcontinent passing through
424 Himalayas, which was also reported by Yin et al. (2017) during springtime from 2011 to 2015. In
425 Figure S8 and 10, WPSCF and WCWT analysis told us that the high O_3 concentration at above heights
426 potentially sourced from northern India, central Pakistan, Nepal, western Bhutan and northern
427 Bangladesh through long-range transport. It should be noted that the potential contribution to O_3 at
428 NAMORS at 200 m from above potential source areas were all over 40 ppb. These contributions from
429 the mentioned potential source areas at other four heights were also over 20-30 ppb. The massive fire
430 emissions during springtime were an important source of O_3 in south Asia (Jena et al., 2015), and the
431 obvious burning during the observation was observed in Figure S9. Moreover, the abundant precursors
432 and high photochemical activity were another significant sources of O_3 in south Asia (Kumar et al.,
433 2012; Sharma et al., 2017).

434 In addition, several previous studies have revealed that the stratospheric O_3 intrusion events were
435 frequent in the Himalayas during spring and summer (Cristofanelli et al., 2010; Chen et al., 2011;
436 Škerlak et al., 2014; Putero et al., 2016). The O_3 invading from stratosphere also contributed to the O_3
437 at NAMORS through long-range transport. Figure 10 showed that the contribution of O_3 transported
438 from Himalayas can even up to 50 ppb, especially under 600 m.

439 Table 3. Trajectory ratios and averaged O_3 concentration for all trajectory clusters arriving in Nam Co
440 at 200 m, 600 m, 1000 m, 1400 m and 1800 m from May to July 2019.

	Cluster	Traj_ratio	O_3 concentration (ppb) Mean$\pm$SD
200 m	1	55.86%	61.50 ± 18.15
	2	11.85%	54.57 ± 14.67
	3	32.28%	65.48 ± 17.41
	All	100.00%	61.14 ± 17.74
600 m	1	62.55%	54.67 ± 6.94
	2	14.32%	50.43 ± 6.64
	3	23.13%	53.27 ± 7.63
	All	100.00%	53.39 ± 7.26
1000 m	1	49.16%	51.61 ± 3.84
	2	8.81%	49.60 ± 3.99
	3	42.03%	51.51 ± 4.50
	All	100.00%	50.98 ± 4.30
1400 m	1	80.14%	50.51 ± 2.89
	2	4.95%	49.12 ± 2.73
	3	14.92%	49.44 ± 3.85
	All	100.00%	50.07 ± 3.15
1800 m	1	83.75%	49.68 ± 2.55
	2	0.00%	49.07 ± 2.23
	3	16.25%	49.69 ± 2.21
	All	100.00%	49.59 ± 2.49

441
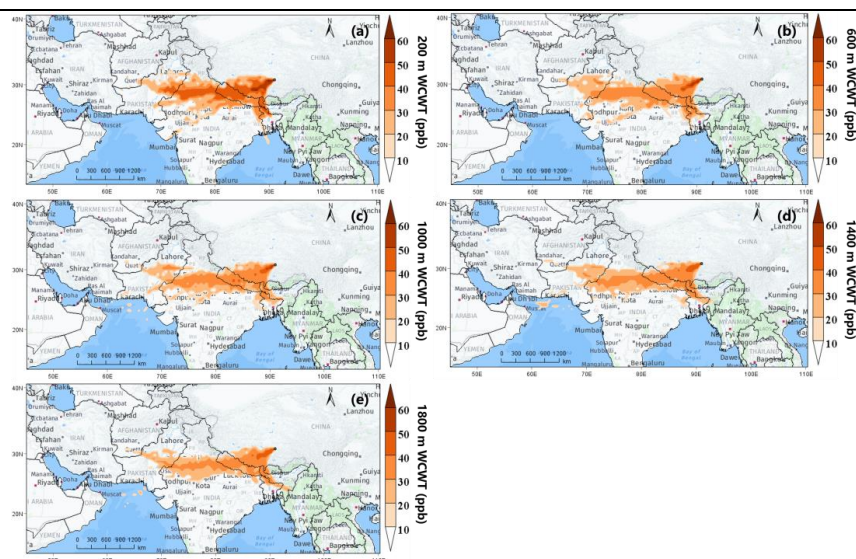
442

443 Figure 10. Spatial distributions of WCWT values for O_3 at (a) 200 m, (b) 600 m, (c) 1000 m, (d) 1400
444 m, and (e) 1800 m height layers from 01st May to 09th July 2019 over CAS (NAMORS).

5 Summary and conclusions

446 MAX-DOAS measurements were performed to clarify the vertical distributions of several atmospheric
447 components (aerosol, H_2O, NO_2, HONO and O_3), and to explore the AOC in vertical space in Nam Co
448 from May to July 2019. The MAX-DOAS NO_2, HONO and O_3 agreed well with in situ measurements,
449 with correlation coefficients of 0.91, 0.62 and 0.82, respectively. We found that the averaged vertical
450 profiles of aerosol, H_2O, HONO and O_3 all exhibited an exponential shape, while NO_2 showed a
451 Gaussian shape with a maximum value of 0.32 ppb appearing at 300-400 m. The maximum
452 concentrations of monthly averaged aerosol (0.17 km^{-1}) and O_3 (66.71 ppb) appeared on May, H_2O
453 (3.68×10^{17} molec cm^{-3}) and HONO (0.13 ppb) appeared on July, and NO_2 (0.39 ppb) occurred on
454 June. For the diurnal variation, above five species all mainly distributed under 1.0 km, and mostly
455 exhibited a multi-peak pattern considering the effect of regional transport and local chemical reaction.

456 O_3 and HONO were the main source of OH on the TP. The diurnal averaged OH production rate from
457 HONO during the observation exhibited a multi-peak pattern appearing before 10:00, 15:00-16:00 and
458 after 19:00 under 0.4 km with the maximum value of 0.81 ppb/h. The OH production rate from O_3
459 shown a unimodal pattern occurring at 13:00-15:00 under 0.4 km with the maximum value of 6.20
460 ppb/h which was obviously higher than that at low-altitude areas. In addition to direct emission, the
461 heterogeneous reaction of NO_2 on wet surfaces was also an important source of HONO in Nam Co. We
462 found that $HONO/NO_2$ first increasing and then decreasing with the increasing of water vapor. The
463 maximum value of $HONO/NO_2$ appeared around water vapor being around 1.0×10^{17} molec cm^{-3}
464 under 1.0 km, and being around $1.0-2.0 \times 10^{17}$ molec cm^{-3} at 1.0-2.0 km height layer. Moreover, high
465 values of $HONO/NO_2$ usually accompanied by high aerosol extinction. O_3 under 2.0 km were
466 potentially sourced from Himalayas, northern India, central Pakistan, Nepal, western Bhutan and
467 northern Bangladesh through long-range transport. Our results draw a picture of further understanding
468 the spatial and temporal variations in oxidation chemistry under PBL and provided a new perspective
469 for source analysis of major atmospheric components through vertical observation on the TP.

Acknowledgements

471 We firstly would like to thank @Tibet group for effectively organizing the Nam Co observation. We
472 also would like to thank Peking University (Chunxiang Ye's group) and Anhui Institute of Optics and
473 Fine Mechanics (Weixiong Zhao's group) to provide the DOAS validation data of HONO, O_3 and NO_2.

474 We thank the National Oceanic and Atmospheric Administration (NOAA) Air Resources Laboratory
475 (ARL) for providing the open HYSPLIT transport and dispersion model. This study was supported by
476 the National Natural Science Foundation of China (42225504 and U21A2027), the Anhui Provincial
477 Natural Science Foundation (2108085QD180), and the Presidential Foundation of the Hefei Institutes
478 of Physical Science, Chinese Academy Sciences (YZJJ2021QN06).

479 **Compliance with ethics guidelines**

480 All authors declare that they have no conflict of interest or financial conflicts to disclose.

481

482 **References**
483 [1] Kang, S., Chen, P., Li, C., Liu, B., and Cong, Z.: Atmospheric Aerosol Elements over the Inland Tibetan Plateau:
484 Concentration, Seasonality, and Transport, Aerosol Air Qual. Res., 16: 789–800, doi: 10.4209/aaqr.2015.05.0307,
485 2016.
486 [2] Xia, X., Zong, X., Cong, Z., Chen, H., Kang, S., and Wang, P.: Baseline continental aerosol over the central
487 Tibetan plateau and a case study of aerosol transport from South Asia, Atmos. Environ., 45, 7370-7378, doi:
488 10.1016/j.atmosenv.2011.07.067, 2011.
489 [3] Xing, C., Liu, C., Wang, S., Hu, Q., Liu, H., Tan, W., Zhang, W., Li, B., and Liu, J.: A new method to determine
490 the aerosol optical properties from multiple-wavelength O_4 absorption by MAX-DOAS observation, Atmos. Meas.
491 Tech., 12, 3289-3302, doi.org/10.5194/amt-12-3289-2019, 2019.
492 [4] Zhao, F., Liu, C., Cai, Z., Liu, X., Bak, J., Kim, J., Hu, Q., Xia, C., Zhang, C., Sun, Y., Wang, W., and Liu, J.:
493 Ozone profile retrievals from TROPOMI: Implication for the variation of tropospheric ozone during the outbreak of
494 COVID-19 in China, Sci. Total Environ., 764, 142886, doi.org/10.1016/j.scitotenv.2020.142886, 2021.
495 [5] Fang, B., Zhao, W., Xu, X., Zhou, J., Ma, X., Wang, S., Zhang, W., Venables, D.S., and Chen, W.: Portable
496 broadband cavity-enhanced spectrometer utilizing Kalman filtering: application to real-time, in situ monitoring of
497 glyoxal and nitrogen dioxide, 25(22), 26910-26922, doi.org/10.1364/OE.25.026910, 2017.
498 [6] Kleffmann, J., Wiesen, P.: Technical Note: Quantification of interferences of wet chemical HONO LOPAP
499 measurements under simulated polar conditions, Atmos. Chem. Phys., 8, 6813-6822,
500 doi.org/10.5194/acp-8-6813-2008, 2008.
501 [7] Bessho, K., Date, K., Hayashi, M., Ikeda, A., Imai, T., Inoue, H., Kumagai, Y., Miyakawa, T., Murata, H., Ohno,
502 T., Okuyama, A., Oyama, R., Sasaki, Y., Shimazu, Y., Shimoji, K., Sumida, Y., Suzuki, M., Taniguchi, H.,
503 Tsuchiyama, H., Uesawa, D., Yokota, H., and Yoshida, R.: An Introduction to Himawari-8/9----Japan's
504 New-Generation Geostationary Meteorological Satellites, Journal of the Meteorological Society of Japan, 94(2),
505 151-183, doi: 10.2151/jmsj.2016-009, 2016.
506 [8] Veefkind, J.P., de Haan, J.F., Brinksma, E.J., Kroon, M., and Levelt, P.F.: Total Ozone From the Ozone
507 Monitoring Instrument (OMI) Using the DOAS Technique, IEEE T. Geosci. Remote., 44(5), 1239-1244, doi:
508 10.1109/TGRS.2006.871204, 2004.
509 [9] Griffin, D., Zhao, X., Mclinden, C.A., Boersma, F., Bourassa, A., Dammers, E., Degenstein, D., Eskes, H., Fehr,
510 L., Fioletov, V., Hayden, K., Kharol, S.K., Li, S., Makar, P., Martin, R.V., Mihele, C., Mittermeier, R.L., Krotkov, N.,
511 Sneep, M., Lamsal, L.N., ter Linden, M., van Geffen, J., Veefkind, P., and Wolde, M.: High-Resolution Mapping of
512 Nitrogen Dioxide With TROPOMI: First Results and Validation Over the Canadian Oil Sands, Geophys. Res, Lett.,
513 46, 1049-1060, doi: 10.1029/2018GL081095, 2018.
514 [10] Su, W., Liu, C., Chan, K.L., Hu, Q., Liu, H., Ji, X., Zhu, Y., Liu, T., Zhang, C., Chen, Y., and Liu, J.: An
515 improved TROPOMI tropospheric HCHO retrieval over China, Atmos. Meas. Tech., 13, 6271-6292,
516 doi.org/10.5194/amt-13-6271-2020, 2020.
517 [11] Grell, G.A., Peckham, S.E., Schmitz, R., McKeen, S.A., Frost, G., Skamarock, W.C., and Eder, B.: Fully coupled
518 "online" chemistry with the WRF model, Atmos, Environ., 39(37), 6957-6975,
519 doi.org/10.1016/j.atmosenv.2005.04.027, 2005.
520 [12] Shi, G., Yang, L., Wang, Y., Kobayashi, K., Zhu, J., Tang, H., Pan, S., Chen, T., Liu, G., and Wang, Y.: Impact
521 of elevated ozone concentration on yield of four Chinese rice cultivars under fully open-air filed conditions, Agr.
522 Ecosys. Environ., 131(3-4), 178-184, doi:10.1016/j.agee.2009.01.009, 2009.
523 [13] Yin, X., Kang, S., de Foy, B., Cong, Z., Luo, J., Zhang, L., Ma, Y., Zhang, G., Rupakheti, D., and Zhang, Q.:
524 Surface ozone at Nam Co in the inland Tibetan Plateau: variation, synthesis comparison and regional
525 representativeness, Atmos. Chem. Phys., 17, 11293-11311, doi.org/10.5194/acp-17-11293-2017, 2017.
526 [14] Draxler, R.R., Hess, G.: An overview of the HYSPLIT_4 modelling system for trajectories, Aust. Meteorol. Mag.,
527 47, 295-308, 1998.
528 [15] Hong, Q., Liu, C., Hu, Q., Xing, C., Tan, W., Liu, H., Huang, Y., Zhu, Y., Zhang, J., Geng, T., and Liu, J.:
529 Evolution of the vertical structure of air pollutants during winter heavy pollution episodes: The role of regional
530 transport and potential sources, Atmos. Res., 228, 106-222, doi.org/10.1016/j.atmosres.2019.05.016, 2019.

[16] Ou, J., Hu, Q., Liu, H., Hong, Q., Xing, C., Tan, W., Lin, H., Wang, X., Xu, H., Zhu, P., and Liu, W.: Vertical characterization and potential sources of aerosols in different seasons over the Yangtze River Delta using ground-based MAX-DOAS, Environ. Pollut., 279, 116898, doi.org/10.1016/j.envpol.2021.116898, 2021.

[17] Hsu, Y.K., Holsen, T.M., Hopke, P.K.: Comparison of hybrid receptor models to locate PCB sources in Chicago, Atmos. Environ., 37, 545-562, doi.org/10.1016/S1352-2310(02)00886-5, 2003.

[18] Wang, Y., Zhang, X., Draxler, R.R.: TrajStat: GIS-based software that uses various trajectory statistical analysis methods to identify potential sources from long-term air pollution measurement data, Environ. Model Softw., 24, 938-939, doi.org/10.1016/j.envsoft.2009.01.004, 2009.

[19] Ye, C.: The first constraint of atmospheric oxidative capacity in Namco, a background Tibetan Plateau research site, AGU Fall Meeting Abstracts, 2019:A51C-08, 2019.

[20] Lin, W., Zhu, T., Song, Y., Zou, H., Tang, M., Tang, X., and Hu, J.: Photolysis of surface O_3 and production potential of OH radicals in the atmosphere over the Tibetan Plateau, J. Geophys. Res.-Atmos., 113, D02309, doi:10.1029/2007JD008831, 2008.

[21] Michoud, V., Kukui, A., Camredon, M., Colomb, A., Borbon, A., Miet, K., Aumont, B., Beekmann, M., Durand-Jolibois, R., Perrier, S., Zapf, P., Siour, G., Ait-Helal, W., Locoge, N., Sauvage, S., Afif, C., Gros, C., Furger, M., Ancellet, G., and Doussin, J.F.: Radical budget analysis in a suburban European site during the MEGAPOLI summer field campaign, Atmos. Chem. Phys., 12, 11951-11974, doi.org/10.5194/acp-12-11951-2012, 2012.

[22] Ryan, R.G., Rhodes, S., Tully, M., Wilson, S., Jones, N., Frieß, U., and Schofield, R.: Daytime HONO, NO_2 and aerosol distributions from MAX-DOAS observations in Melbourne, Atmos. Chem. Phys., 18, 13969-13958, doi.org/10.5194/acp-18-13969-2018, 2018.

[23] Xue, C., Zhang, C., Ye, C., Liu, P., Catoire, V., Krysztofiak, G., Chen, H., Ren, Y., Zhao, X., Wang, J., Zhang, F., Zhang, C., Zhang, J., An, J., Wang, T., Chen, J., Kleffmann, J., Mellouki, A., and Mu, Y.: HONO budget and its role in nitrate formation in rural North China Plain, Environ. Sci. Tech., 54, 18, 11048-11057, doi.org/10.1021/acs.est.0c01832, 2020.

[24] Xing, C., Liu, C., Wu, H., Lin, J., Wang, F., Wang, S., and Gao, M.: Ground-based vertical profile observations of atmospheric composition on the Tibetan Plateau (2017-2019), Earth Syst. Sci. Data, 13, 4897-4912, doi.org/10.5194/essd-13-4897-2021, 2021a.

[25] Xing, C., Liu, C., Hu, Q., Fu, Q., Wang, S., Lin, H., Zhu, Y., Wang, S., Wang, W., Javed, Z., Ji, X., Liu, J.: Vertical distributions of wintertime atmospheric nitrogenous compounds and the corresponding OH radicals production in Leshan, southwest China, J. Environ. Sci., 105, 44-55, doi.org/10.1016/j.jes.2020.11.019.

[26] Luo, S., Holland, F., Rohrer, F., Lu, K., Bohn, B., Brauers, T., Chang, C.C., Fuchs, H., Häseler, R., Kita, K., Kondo, Y., Li, X., Shao, M., Zeng, L., Wahner, A., Zhang, Y., Wang, W., Hofzumahaus, A.: Atmospheric OH reactivities in the Pearl River Delta-China in summer 2006: measurement and model results, Atmos. Chem. Phys., 10, 11243-11260, doi.org/10.5194/acp-10-11243-2010, 2010.

[27] Yang, Y., Wang, Y., Huang, W., Yao, D., Zhao, S., Wang, Y., Ji, D., Zhang, R., Wang, Y.: Parameterized atmospheric oxidation capacity and speciated OH reactivity over a suburban site in the North China Plain: A comparative study between summer and winter, Sci. Total Environ., 773, 145264, doi.org/10.1016/j.scitotenv.2021.145264, 2021.

[28] Ma, Y., Zhong, L., Su, Z.: Energy and water cycles in the third pole, Water, 14(7), 1175, doi.org/10.3390/w14071175, 2022.

[29] Kang, S., Zhang, Y., Chen, P., Guo, J., Zhang, Q., Cong, Z., Kaspari, S., Tripathee, L., Gao, T., Niu, H., Zhong, X., Chen, X., Hu, Z., Li, X., Li, Y., Neupane, B., Yan, F., Rupakheti, D., Gul, C., Zhang, W., Wu, G., Yang, L., Wang, Z., Li, C.: Black carbon and organic carbon dataset over the Third Pole, Earth Syst. Sci. Data, 14, 683–707, doi.org/10.5194/essd-14-683-2022, 2022.

[30] Ma, Y., Hu, Z., Xie, Z., Ma, W., Wang, B., Chen, X., Li, M., Zhong, L., Sun, F., Gu, L., Han, C., Zhang, L., Liu, X., Ding, Z., Sun, G., Wang, S., Wang, Y., and Wang, Z.: A long-term (2005–2016) dataset of integrated land-atmosphere interaction observations on the Tibetan Plateau, V1, Science Data Bank, 2020.

[31] Qu, B., Zhang, Y., Kang, S., Sillanpää, M.: Water quality in the Tibetan Plateau: Major ions and trace elements in rivers of the "Water Tower of Asia", Sci. Total Environ., 649, 571-581, doi.org/10.1016/j.scitotenv.2018.08.316, 2019.

[32] Zhou, S., Sun, F., Wang, M., Zhou, S., and Qing, Y.: Effects of atmospheric heat source on the Tibetan Plateau vortex in different stages: A case study in June 2016, Atmosphere, 13(5), 689, doi.org/10.3390/atmos13050689, 2022.

[33] Liu, J., Guan, X., Gao, Z., Huang, X., Ma, J., He, Y., and Xie, T.: Inter-decadal variability of the heat source over the Tibetan Plateau, Clim. Dynam., 58, 729-739, doi.org/10.1007/s00382-021-05929-z, 2022.

[34] Chen, P., Kang, S., Bai, J., Sillanpää, M., Li, C.: Yak dung combustion aerosols in the Tibetan Plateau: Chemical characteristics and influence on the local atmospheric environment, Atmos. Res., 156, 58-66, doi.org/10.1016/j.atmosres.2015.01.001, 2015.

[35] Boos, W. R. and Kuang, Z.: Dominant control of the South Asian monsoon by orographic insulation versus plateau heating, Nature, 463, 218–222, 2010.

[36] Yanai, M., Li, C., and Song, Z.: Seasonal Heating of the Tibetan Plateau and Its Effects on the Evolution of the Asian Summer Monsoon, J. Meteorol. Soc. Jpn. Ser. II, 70, 319–351, 1992.

592   [37] Li, C., Zou, Q., Xu, X., and Gao, S.: Water vapor transport around the Tibetan Plateau and its effect on summer
593   rainfall over the Yangtze River valley, J. Meteorol. Res., 30, 472-482, doi: 10.1007/s13351-016-5123-1, 2016.
594   [38] Lei, Y., Zhu, Y., Wang, B., Yao, T., Yang, K., Zhang, X., Zhai, J., and Ma, N.: Extreme lake level changes in the
595   Tibetan Plateau associated with the 2015/2016 El Niño, Geophys. Res. Lett., 46, 11, 5889-5898,
596   doi.org/10.1029/2019GL081946, 2019.
597   [39] Hsu, H-H., and Liu, X.: Relationship between the Tibetan Plateau heating and East Asian summer monsoon
598   rainfall, Res. Lett., 30, 20, doi.org/10.1029/2003GL017909, 2003.
599   [40] Zhang, L., Guo, X., Zhao, T., Gong, S., Xu, X., Li, Y., Luo, L., Gui, K., Wang, H., Zheng, Y., and Yin, X.: A
600   modelling study of the terrain effects on the haze pollution in Sichuan Basin, Atmos. Environ., 196, 77-85,
601   doi.org/10.1016/j.atmosenv.2018.10.007, 2019.
602   [41] Barnett, T. P., Adam, J. C., and Lettenmaier, D. P.: Potential impacts of a warming climate on water availability
603   in snow-dominated regions, Nature, 438, 303–309, 2005.
604   [42] Bolch, T., Kulkarni, A., Kaab, A., Huggel, C., Paul, F., Cogley, J. G., Frey, H., Kargel, J. S., Fujita, K., Scheel,
605   M., Bajracharya, S., and Stoffel, M.: The State and Fate of Himalayan Glaciers, Science, 336, 310–314, 2012.
606   [43] Cong, Z., Kang, S., Kawamura, K., Liu, B., Wan, X., Wang, Z., Gao, S., and Fu, P.: Carbonaceous aerosols on
607   the south edge of the Tibetan Plateau: concentrations, seasonality and sources, Atmos. Chem. Phys., 15, 1573–1584,
608   https://doi.org/10.5194/acp-15-1573-2015, 2015.
609   [44] Kang, S. C., Huang, J., Wang, F. Y., Zhang, Q. G., Zhang, Y. L., Li, C. L., Wang, L., Chen, P. F., Sharma, C. M.,
610   Li, Q., Sillanpaa, M., Hou, J. Z., Xu, B. Q., and Guo, J. M.: Atmospheric Mercury Depositional Chronology
611   Reconstructed from Lake Sediments and Ice Core in the Himalayas and Tibetan Plateau, Environ. Sci. Technol., 50,
612   2859–2869, 2016.
613   [45] Ran, L., Deng, Z., Wu, Y., Li, J., Bai, Z., Lu, Y., Zhuoga, D., and Bian J.: Measurement report: Vertical
614   profiling of particle size distributions over Lhasa, Tibet – tethered balloon-based in situ measurements and source
615   apportionment, Atmos. Chem. Phys., 22, 6217–6229, doi.org/10.5194/acp-22-6217-2022, 2022.
616   [46] Wang, K., Hattori, S., Lin, M., Ishino, S., Alexander, B., Kamezaki, K., Yoshida, N., and Kang, S.: Isotopic
617   constraints on atmospheric sulfate formation pathways in the Mt. Everest region, southern Tibetan Plateau, Atmos.
618   Chem. Phys., 21, 8357–8376, https://doi.org/10.5194/acp-21-8357-2021, 2021.
619   [47] Che, J. and Zhao, P.: Characteristics of the summer atmospheric boundary layer height over the Tibetan Plateau
620   and influential factors, Atmos. Chem. Phys., 21, 5253–5268, https://doi.org/10.5194/acp-21-5253-2021, 2021.
621   [48] Sun, Y., Yin, H., Cheng, Y., Zhang, Q., Zheng, B., Notholt, J., Lu, X., Liu, C., Tian, Y., Liu, J.: Quantifying
622   variability, source, and transport of CO in the urban areas over the Himalayas and Tibetan Plateau, Atmos. Chem.
623   Phys., 21, 9201–9222, https://doi.org/10.5194/acp-21-9201-2021, 2021.
624   [49] Li, R., Zhao, Y., Zhou, W., Meng, Y., Zhang, Z., and Fu, H.: Developing a novel hybrid model for the estimation
625   of surface 8-h ozone (O_3) across the remote Tibetan Plateau during 2005-2018, Atmos. Chem. Phys., 20, 6159–6175,
626   https://doi.org/10.5194/acp-20-6159-2020.
627   [50] Gao, M., Gao, J., Zhu, B., Kumar, R., Lu, X., Song, S., Zhang, Y., Jia, B., Wang, P., Beig, G., Hu, J., Ying, Q.,
628   Zhang, H., Sherman, P., and McElroy, M. B.: Ozone pollution over China and India: seasonality and sources, Atmos.
629   Chem. Phys., 20, 4399–4414, https://doi.org/10.5194/acp-20-4399-2020, 2020.
630   [51] Rawat, P., and Naja, M.: Remote sensing study of ozone, NO_2, and CO: some contrary effects of SARS-CoV-2
631   lockdown over India, Environ. Sci. Pollut. R., 29, 22515-22530, 2022.
632   [52] Huang, J., Minnis, P., Yi, Y., Tang, Q., Wang, X., Hu, Y., Liu, Z., Ayers, K., Trepte, C., and Winker, D.:
633   Summer dust aerosols detected from CALIPSO over the Tibetan Plateau, Geophys. Res. Lett., 34, L18805,
634   https://doi.org/10.1029/2007GL029938, 2007.
635   [53] Li, R., Zhao, Y., Zhou, W., Meng, Y., Zhang, Z., and Fu, H.: Developing a novel hybrid model for the estimation
636   of surface 8 h ozone (O3) across the remote Tibetan Plateau during 2005–2018, Atmos. Chem. Phys., 20, 6159–6175,
637   https://doi.org/10.5194/acp-20-6159-2020, 2020.
638   [54] Zhu, J., Xia, X., Che, H., Wang, J., Cong, Z., Zhao, T., Kang, S., Zhang, X., Yu, X., and Zhang, Y.:
639   Spatiotemporal variation of aerosol and potential long-range transport impact over the Tibetan Plateau, China, Atmos.
640   Chem. Phys., 19, 14637–14656, https://doi.org/10.5194/acp-19-14637-2019, 2019.
641   [55] Xu, X., Sun, C., Chen, D., Zhao, T., Xu, J., Zhang, S., Li, J., Chen, B., Zhao, Y., Xu, H., Dong, L., Sun, X., and
642   Zhu, Y.: A vertical transport window of water vapor in the troposphere over the Tibetan Plateau with implications for
643   global climate change, Atmos. Chem. Phys., 22, 1149–1157, https://doi.org/10.5194/acp-22-1149-2022, 2022.
644   [56] Xu, X., Wu, H., Yang, X., and Xie, L.: Distribution and transport characteristics of dust aerosol over Tibetan
645   Plateau and Taklimakan Desert in China using MERRA-2 and CALIPSO data, Atmos. Environ., 237, 117670,
646   https://doi.org/10.1016/j.atmosenv.2020.117670, 2020.
647   [57] Yang, K., Koike, T., and Yang, D.: Surface flux parameterization in the Tibetan Plateau, Bound.-Lay. Meteorol.,
648   106, 245–262, 2003.
649   [58] Seidel, D. J., Ao, C. O., and Li, K.: Estimating climatological planetary boundary layer heights from radiosonde
650   observations: Comparison of methods and uncertainty analysis, J. Geophys. Res., 115, D16113,
651   https://doi.org/10.1029/2009JD013680, 2010.

[59] Dong, Q., Huang, Z., Li, W., Li, Z., Song, X., Liu, W., Wang, T., Bi, J., and Shi, J.: Polarization lidar measurements of dust optical properties at the junction of the Taklimakan Desert-Tibetan Plateau, Remote Sens., 14(3), 558, https://doi.org/10.3390/rs14030558, 2022.

[60] Zhang, J., Xia, X., and Wu, X.: First in situ UV profile across the UTLS accompanied by ozone measurement over the Tibetan Plateau, J. Environ., Sci., 98, 71–76, 2020.

[61] Fang, X., Li, T., Ban, C., Wu, Z., Li, J., Li, F., Cen, Y., and Tian, B.: A mobile differential absorption lidar for simultaneous observations of tropospheric and stratospheric ozone over Tibet, Opt. Express, 27, 4126–4139, 2019.

[62] Wang, Y., Pukite, J., Wagner, T., Donner, S.; Beirle, S., Hilboll, A., Vrekoussis, M., Richter, A., Apituley, A., Piters, A., Allaart, M., Eskes, H., Frumau, A., van Roozendael, M., Lampel, J., Platt, U., Schmitt, S., Swart, D., and Vonk, J.: Vertical profiles of tropospheric ozone from MAX-DOAS measurement during the CINDI-2 campaign: part 1—Development of a new retrieval algorithm. J. Geophys. Res. Atmos. 123 (18), 10–637. https://doi.org/10.1029/2018JD028647, 2018.

[63] Xing, C., Liu, C., Wang, S., Chan, K.L., Gao, Y., Huang, X., Su, W., Zhang, C., Dong, Y., Fan, G., Zhang, T., Chen, Z., Hu, Q., Su, H., Xie, Z., and Liu, J.: Observations of the vertical distributions of summertime atmospheric pollutants and the corresponding ozone production in Shanghai, China. Atmos. Chem. Phys. 17, 14275–14289. https://doi.org/10.5194/acp-17-14275-2017, 2017.

[64] Xing, C., Liu, C., Wang, S., Hu, Q., Liu, H., Tan, W., Zhang, W., Li, B., and Liu, J.; A new method to determine the aerosol optical properties from multiple-wavelength O_4 absorptions by MAX-DOAS observation. Atmos. Meas. Tech. 12, 3289–3302. https://doi.org/10.5194/amt-12-3289-2019, 2019.

[65] Xing, C., Liu, C., Hu, Q., Fu, Q., Lin, H., Wang, S., Su, W., Wang, W., Javed, Z., and Liu, J.: Identifying the wintertime sources of volatile organic compounds (VOCs) from MAX-DOAS measured formaldehyde and glyoxal in Chongqing, Southwest China. Sci. Total Environ. 715, 136258 https://doi.org/10.1016/j.scitotenv.2019.136258, 2020.

[66] Ye, D. Z., and Gao, Y. X.: The Meteorology of the Tibetan Plateau (in Chinese), 278pp., Science Press, Beijing, pp. 39– 48, 1979.

[67] Liu, Y., and Li, W.: Deepening of the ozone valley over Tibetan Plateau and its possible influences (Chinese with English abstract), Acta Meteorologica Sinica, 59(1), 97– 106, 2001.

[68] Yang, J., Kang, S., Hu, Y., Chen, X., Rai, M.: Influence of South Asian biomass burning on ozone and aerosol concentrations over the Tibetan Plateau, Adv. Atmos. Sci., 39, 1184-1197, 2022.

[69] Yu, J., Meng, L., Chen, Y., Zhang, H., and Liu, J.: Ozone profiles, precursors, and vertical distribution in urban Lhasa, Tibetan Plateau, Remote Sens., 14(11), 2533, https://doi.org/10.3390/rs14112533, 2022.

[70] Li, M., Mao, J., Chen, S., Bian, J., Bai, Z., Wang, X., Chen, W., and Yu, P.: Significant contribution of lightning NO_x to summertime surface O_3 on the Tibetan Plateau, Sci, Total, Environ., 829, 154639, doi.org/10.1016/j.scitotenv.2022.154639, 2022.

[71] Zhou, L., Zhang, X., Zhang, J.: Temporal and spatial distributions of atmospheric hydroxyl radicals based on the observation with the aura microwave limb sounder. Science & Technology Review, 33(17): 69-77, 2015.

[72] Yin, X., Kang, S., de Foy, B., Cong, Z., Luo, J., Zhang, L., Ma, Y., Zhang, G., Rupakheti, D., and Zhang, Q.: Surface ozone at Nam Co in the inland Tibetan Plateau: variation, synthesis comparison and regional representativeness, Atmos. Chem. Phys., 17, 11293–11311, https://doi.org/10.5194/acp-17-11293-2017, 2017.

[73] Xu, X., Zhang, H., Lin, W., Wang, Y., Xu, W., and Jia, S.: First simultaneous measurements of peroxyacetyl nitrate (PAN) and ozone at Nam Co in the central Tibetan Plateau: impacts from the PBL evolution and transport processes, Atmos. Chem. Phys., 18, 5199–5217, https://doi.org/10.5194/acp-18-5199-2018, 2018.

[74] Bi, H., Chen, S., Zhao, D., Lu, F., Chen, Y., and Guan, Y.: Aerosol optical properties and its direct radiative forcing over Tibetan Plateau from 2006 to 2017, Particuology, 74, 64-73, https://doi.org/10.1016/j.partic.2022.05.007, 2023.

[75] Yang, J., Kang, S., and Ji, Z.: Critical contribution of south Asian residential emissions to atmospheric black carbon over the Tibetan plateau, Sci. Total Environ., 709, 135923, https://doi.org/10.1016/j.scitotenv.2019.135923, 2020.

[76] Zhang, X., Ming, J., Li, Z., Wang, F., and Zhang, G.: The online measured black carbon aerosol and source orientations in the Nam Co region, Tibet, Environ. Sci. Pollut. Res., 24, 25021-25033, doi: 10.1007/s11356-017-0165-1, 2017.

[77] Yang, J., Duan, K., Kang, S., Shi, P., and Ji, Z.: Potential feedback between aerosols and meteorological conditions in a heavy pollution event over the Tibetan Plateau and Indo-Gangetic Plain, Clim. Dyn., 48(9), 2901-2917, doi:10.1007/s00382-016-3240-2, 2017.

[78] Wan, X., Kang, S., Wang, Y., Xin, J., Liu, B., Guo, Y., Wen, T., Zhang, G., and Cong, Z.: Size distribution of carbonaceous aerosols at a high-altitude site on the central Tibetan Plateau (Nam Co Station, 4730 m a.s.l.), Atmos. Res, 153, 155-164, doi:10.1016/j.atmosres.2014.08.008, 2015.

[79] Li, C., Bosch, C., Kang, S., Andersson, A., Chen, P., Zhang, Q., Cong, Z., Chen, B., Qin, D., and Gustafsson, O.: Sources of black carbon to the Himalayan-Tibetan Plateau glaciers, Nat. Commun., 7, 12574, doi:10.1038/ncomms12574, 2016.

[80] Lei, Y., Yang, K., Wang, B., Sheng, Y., Bird, B.W., Zhang, G., and Tian, L.: Response of inland lake dynamics over the Tibetan Plateau to climate change, Clim. Chang, 125, 281-290, doi:10.1007/210584-014-1175-3, 2014.

[81] Zhu, G., Guo, H., Qin, D., Pan, H., Jia, W., and Ma, X.: Contribution of recycled moisture to precipitation in the monsoon marginal zone: Estimate based on stable isotope data, J. Hydrol., 569, 423-435, doi:10.1016/j.jhydrol.2018.12.014, 2019.

[82] Boxe, C.: Nitrate photochemistry and interrelated chemical phenomena in ice[M]. California Institute of Technology, 2005.

[83] Xu, R., Tie, X., Li, G., Zhao, S., Cao, J., Feng, T., and Long, X.: Effect of biomass burning on black carbon (BC) in South Asia and Tibetan Plateau: The analysis of WRF-Chem modeling, Sci. Total Environ., 645, 901-912, doi:10.1016/j.scitotenv.2018.07.165, 2018.

[84] Neupane, B., Kang, S., Chen, P., Zhang, Y., Ram, K., Rupakheti, D., Tripathee, L., Sharma, C.M., Cong, Z., Li, C., Hou, J., Xu, M., and Thapa, P.: Historical black carbon reconstruction from the lake sediments of the Himalayan-Tibetan Plateau, Environ. Sci. Tech., 53, 5641-5651, doi:10.1021/acs.est.8b07025, 2019.

[85] Xu, K., Zhong, L., Ma, Y., Zou, M., and Huang, Z.: A study on the water vapor transport trend and water vapor sources of the Tibetan Plateau, Theor. Appl. Climatol., 140, 1031-1042, doi:10.1007/s00704-020-03142-2, 2020.

[86] Xu, Y., Kang, S., Zhang, Y., and Zhang, Y.: A method for estimating the contribution of evaporative vapor from Nam Co to local atmospheric vapor based on stable isotopes of water bodies, Chinese Sci. Bull., 56(14), 1511-1517, doi:10.1007/s11434-011-4467-2, 2011.

[87] Chen, P., Kang, S., Yang, J., Pu, T., Li, C., Guo, J., and Tripathee, L.: Spatial and temporal variations of gaseous and particle pollutants in six sites in Tibet, China, during 2016-2017, Aerosol Air Qual. Res., 19, 516-527, doi:10.4209/aaqr.2018.10.0360, 2019.

[88] Wang, T., Xue, L., Brimblecombe, P., Lam, Y, Li, L. and Zhang, L.: Ozone pollution in China: A review of concentrations, meteorological influences, chemical precursors, and effects. Sci. Total Environ., 575, 1582–1596, doi:10.1016/j.scitotenv.2016.10.081, 2017.

[89] Pokharel, M., Guang, J., Liu, B., Kang, S., Ma, Y., Holben, B.N., Xia, X., Xin, J., Ram, K., Rupakheti, D., Wan, X., Wu, G., Bhattarai, H., Zhao, C., and Cong, Z.: Aerosol properties over Tibetan Plateau from a decade of AERONET measurements: Baseline, types, and influencing factors, J. Geophys. Res.: Atmos., 124, 13357-13374, doi:10.1029/2019JD031293, 2019.

[90] Cong, Z., Kang, S., Smirnov, A., and Holben, B.: Aerosol optical properties at Nam Co, a remote site in central Tibetan Plateau, Atmos. Res, 92, 42-48, doi:10.1016/j.atmosres.2008.08.005, 2009.

[91] Qian, Y., Wang, H., Zhao, C., Zhao, C., Chen, S., Hu, X., and Kang, S.: Understanding third pole atmospheric dynamics and land surface processes and their associations with the cryosphere, air quality, and climate change, Adv. Atmos. Sci., 39, 1017-1020, doi:10.1007/s00376-022-2004-7, 2022.

[92] Xu, L., Liu, H., Du, Q., and Xu, X.: The assessment of the planetary boundary layer schemes in WRF over the central Tibetan Plateau, Atmos. Res., 230, 104644, doi:10.1016/j.atmosres.2019.104644, 2019.

[93] Yang, J., and Duan, K.: Effects of initial drivers and land use on WRF modeling for near-surface fields and atmospheric boundary layer over the northeastern Tibetan Plateau, Adv. Meteorol., 2016, 7849249, doi:10.1155/2016/7849249, 2016.

[94] Kleffmann, J., Gavriloaiei, T., Hofzumahaus, A., Holland, F., Koppmann, R., Rupp, L., Schlosser, E., Siese, M., and Wahner, A.: Daytime formation of nitrous acid: A major source of OH radicals in a forest, Geophys. Res. Lett., 32(5), doi:10.1029/2005GL022524, 2005.

[95] Su, H., Cheng, Y., Shao, M., Gao, D., Yu, Z., Zeng, L., Slanina, J., Zhang, Y., and Wiedensohler, A.: Nitrous acid (HONO) and its daytime sources at a rural site during the 2004 PRIDE-PRD experiment in China, J. Geophys. Res., 113, D14312, doi:10.1029/2007JD009060, 2008.

[96] Yang, Y., Li, X., Zu, K., Lian, C., Chen, S., Dong, H., Feng, M., Liu, H., Liu, J., Lu, K., Lu, S., Ma, X., Song, D., Wang, W., Yang, S., Yang, X., Yu, X., Zhu, Y., Zeng, L., Tan, Q., and Zhang, Y.: Elucidating the effect of HONO and O₃ pollution by a case study in southwest China, Sci. Total Environ., 756, 144127, doi:10.1016/j.scitotenv.2020.144127, 2021.

[97] Liu, T., Hong, Y., Li, M., Xu, L., Chen, J., Bian, Y., Yang, C., Dan, Y., Zhang, Y., Xue, L., Zhao, M., Huang, Z., and Wang, H.: Atmospheric oxidation capacity and ozone pollution mechanism in a coastal city of southeastern China: analysis of a typical photochemical episode by an observation-based model, Atmos. Chem. Phys., 22, 2173-2190, doi:10.5194/acp-22-2173-2022, 2022.

[98] Xu, S., Wang, S., Xia, M., Lin, H., Xing, C., Ji, X., Su, W., Tan, W., Liu, C., and Hu, Q.: Observations by ground-based MAX-DOAS of the vertical characters of winter pollution and the influencing factors of HONO generation in Shanghai, China, Remote Sens., 13, 3518, doi:10.3390/rs13173518, 2021.

[99] Hendrick, F., Müller, J.F., Clémer, K., Wang, P., De Mazière, M., Fayt, C., Gielen, C., Hermans, C., Ma, J., Pinardi, G., Stavrakou, T., Vlemmix, T., Van Roozendael, M.: Four years of ground-based MAX-DOAS observations of HONO and NO2 in the Beijing area, Atmos. Chem. Phys., 14, 765–781, doi:10.5194/acp-14-765-2014, 2014.

[100] Cui, L., Li, R., Fu, H., Li, Q., Zhang, L., George, C., and Chen, J.: Formation features of nitrous acid in the offshore area of the East China Sea, Sci. Total Environ., 682, 138-150, doi: 10.1016/j.scitotenv.2019.05.004, 2019.

[101] Yang, J., Shen, H., Guo, M., Zhao, M., Jiang, Y., Chen, T., Liu, Y., Li, H., Zhu, Y., Meng, H., Wang, W., and Xue, L.: Strong marine-derived nitrous acid (HONO) production observed in the coastal atmosphere of northern China, Atmos. Environ., 244, 117948, doi: 10.1016/j.atmosenv.2020.117948, 2021.

774 [102] Liu, Y., Nie, W., Xu, Z., Wang, T., Wang, R., Li, Y., Wang, L., Chi, X., and Ding, A.: Semi-quantitative
775 understanding of source contribution to nitrous acid (HONO) based on 1 year of continuous observation at the
776 SORPES station in eastern China, Atmos. Chem. Phys., 19, 13289–13308, doi: 10.5194/acp-19-13289-2019, 2019.
777 [103] Jena, C., Ghude, S.D., Pfister, G.G., Chate, D.M., Kumar, R., Beig, G., Surendran, D.E., Fadnavis, S., and Lal,
778 D.M.: Influence of springtime biomass burning in South Asia on regional ozone (O3): A model based case study,
779 Atmos. Environ., 100, 37-47, doi:10.1016/j.atmosenv.2014.10.027, 2015.
780 [104] Xing, L., Bei, N., Guo, J., Wang, Q., Liu, S., Han, Y., Pongpiachan, S., and Li, G.: Impacts of biomass burning
781 in peninsular southeast Asia on PM$_{2.5}$ concentration and ozone formation in southeastern China during springtime-A
782 case study, J. Geophys. Res.: Atmos., 126(22), e2021JD034908, doi:10.1029/2021JD034908, 2021.
783 [105] Kumar, R., Naja, M., Pfister, G.G., Barth, M.C., Wiedinmyer, C., and Brasseur, G.P.: Simulations over South
784 Asia using the Weather Research and Forecasting model with Chemistry (WRF-Chem): chemistry evaluation and
785 initial results, Geosci. Model Dev., 5, 619–648, doi:10.5194/gmd-5-619-2012, 2012.
786 [106] Sharma, A., Ojha, N., Pozzer, A., Mar, K.A., Beig, G., Lelieveld, J., and Gunthe, S.S.: WRF-Chem simulated
787 surface ozone over south Asia during the pre-monsoon: effects of emission inventories and chemical mechanisms,
788 Atmos. Chem. Phys., 17, 14393–14413, doi: 10.5194/acp-17-14393-2017, 2017.
789 [107] Cristofanelli, P., Bracci, A., Sprenger, M., Marinoni, A., Bonafè, U., Calzolari, F., Duchi, R., Laj, P., Pichon, J.
790 M., Roccato, F., Venzac, H., Vuillermoz, E., and Bonasoni, P.: Tropospheric ozone variations at the Nepal Climate
791 ObservatoryPyramid (Himalayas, 5079 m a.s.l.) and influence of deep stratospheric intrusion events, Atmos. Chem.
792 Phys., 10, 6537–6549, doi:10.5194/acp-10-6537-2010, 2010.
793 [108] Chen, X. L., Ma, Y. M., Kelder, H., Su, Z., and Yang, K.: On the behaviour of the tropopause folding events
794 over the Tibetan Plateau, Atmos. Chem. Phys., 11, 5113–5122, doi:10.5194/acp-11-5113-2011, 2011.
795 [109] Škerlak, B., Sprenger, M., and Wernli, H.: A global climatology of stratosphere–troposphere exchange using the
796 ERA-Interim data set from 1979 to 2011, Atmos. Chem. Phys., 14, 913–937, doi:10.5194/acp-14-913-2014, 2014.
797 [110] Putero, D., Cristofanelli, P., Sprenger, M., Škerlak, B., Tositti, L., and Bonasoni, P.: STEFLUX, a tool for
798 investigating stratospheric intrusions: application to two WMO/GAW global stations, Atmos. Chem. Phys., 16,
799 14203–14217, doi:10.5194/acp-16-14203-2016, 2016.
800 [111] Fu, X., Wang, T., Zhang, L., Li, Q., Wang, Z., Xia, M., Yun, H., Wang, W., Yu, C., Yue, D., Zhou, Y., Zheng,
801 J., and Han, R.: The significant contribution of HONO to secondary pollutants during a severe winter pollution event
802 in southern China, Atmos. Chem. Phys., 19, 1–14, doi: 10.5194/acp-19-1-2019, 2019.
803 [112] Ren, Y., Stieger, B., Spindler, G., Grosselin, B., Mellouki, A., Tuch, T., Wiedensohler, A., and Herrmann, H.:
804 Role of the dew water on the ground surface in HONO distribution: a case measurement in Melpitz, Atmos. Chem.
805 Phys., 20, 13069–13089, doi: 10.5194/acp-20-13069-2020, 2020.
806 [113] Crilley, L.R., Kramer, L.J., Pope, F.D., Reed, C., Lee, J.D., Carpenter, L.J., Hollis, L.D.J., Ball, S.M., and Bloss,
807 W.J.: Is the ocean surface a source of nitrous acid (HONO) in the marine boundary layer? Atmos. Chem. Phys., 21,
808 18213–18225, doi: 10.5194/acp-21-18213-2021, 2021.
809 [114] Li, S., Song, W., Zhan, H., Zhang, Y., Zhang, X., Li, W., Tong, S., Pei, C., Wang, Y., Chen, Y., Huang, Z.,
810 Zhang, R., Zhu, M., Fang, H., Wu, Z., Wang, J., Luo, S., Fu, X., Xiao, S., Huang, X., Zeng, J., Zhang, H., Chen, D.,
811 Gligorovski, S., Ge, M., George, C., and Wang, X.: Contribution of vehicle emission and NO$_2$ surface conversion to
812 nitrous acid (HONO) in urban environments: Implications from tests in a tunnel, Environ. Sci. Technol., 55(23),
813 15616-15624, doi:10.1021/acs.est.1c00405, 2021.
814 [115] Chai, J., Dibb, J.E., Anderson, B.E., Bekker, C., Blum, D.E., Heim, E., Jordan, C.E., Joyce, E.E., Kaspari, J.H.,
815 Munro, H., Walters, W.W., and Hastings, M.G.: Isotopic evidence for dominant secondary production of HONO in
816 near-ground wildfire plumes, Atmos. Chem. Phys., 21, 13077–13098, doi: 10.5194/acp-21-13077-2021, 2021.
817 [116] Cui, L., and Wang, S.: Mapping the daily nitrous acid (HONO) concentrations across China during 2006-2017
818 through ensemble machine-learning algorithm, Sci. Total Environ., 785, 147325, doi:10.1016/j.scitotenv.2021.147325,
819 2021.
820 [117] Cui, L., Li, R., Fu, H., Meng, Y., Zhao, Y., Li, Q., and Chen, J.: Nitrous acid emission from open burning of
821 major crop residues in mainland China, Atmos. Environ., 244, 117950, doi:10.1016/j.atmosenv.2020.117950, 2021.
822 [118] Su, H., Cheng, Y., Oswald, R., Behrendt, T., Trebs, I., Meixner, F.X., Andreae, M.O., Cheng, P., Zhang, Y., and
823 Poschl, U.: Soil nitrite as a source of atmospheric HONO and OH radicals, Science, 333(6049), 1616-1618,
824 doi:10.1126/science.1207687, 2011.
825 [119] Lin, F., Liu, C., Hu, X., Fu, Y., Zheng, X., Wang, R., Zhang, W., and Cao, G.: Characterizing nitric oxide
826 emissions from two typical alpine ecosystems, J. Environ. Sci., 77, 312-322, doi:10.1016/j.jes.2018.08.011, 2019.
827 [120] Gil, J., Kim, J., Lee, M., Lee, G., Lee, D., Jung, J., An, J., Hong, J., Cho, S., Lee, J., and Long, R.: The role of
828 HONO in O3 formation and insight into its formation mechanism during the KORUS-AQ Campaign, Atmos. Chem.
829 Phys. Disscu., doi: 10.5194/acp-2019-1012, 2019.
830 [121] Wen, L., Chen, T., Zheng, P., Wu, L., Wang, X., Mellouki, A., Xue, L., and Wang, W.: Nitrous acid marine
831 boundary layer over eastern Bohai Sea, China: Characteristics, sources, and implications, Sci. Total Environ., 670,
832 282-291, doi:10.1016/j.scitotenv.2019.03.225, 2019.

833 [122] Lu, X., Wang, Y., Li, J., Shen, L., and Fung, J.C.H.: Evidence of heterogeneous HONO formation from aerosols
834 and the regional photochemical impact of this HONO source, Environ. Res. Lett. 13, 114002,
835 doi:10.1088/1748-9326aae492, 2018.
836 [123] Cui, L., Li, R., Zhang, Y., Meng, Y., Fu, H., and Chen, J.: An observational study of nitrous acid (HONO) in
837 Shanghai, China: The aerosol impact on HONO formation during the haze episodes, Sci. Total Environ., 630,
838 1057-1070, doi:10.1016/j.scitotenv.2018.02.063, 2018.
839 [124] Wang, S., Zhou, R., Zhao, H., Wang, Z., Chen, L., and Zhou, B.: Long-term observation of atmospheric nitrous
840 acid (HONO) and its implication to local NO_2 levels in Shanghai, China, Atmos. Environ., 77, 718–724,
841 doi:10.1016/j.atmosenv.2013.05.071, 2013.
842 [125] Meng, F., Qin, M., Tang, K., Duan, J., Fang, W., Liang, S., Ye, K., Xie, P., Sun, Y., Xie, C., Ye, C., Fu, P., Liu,
843 J., and Liu, W.: High-resolution vertical distribution and sources of HONO and NO_2 in the nocturnal boundary layer
844 in urban Beijing, China, Atmos. Chem. Phys., 20, 5071–5092, doi: 10.5194/acp-20-5071-2020, 2020.
845 [126] Zhang, W., Tong, S., Jia, C., Wang, L., Liu, B., Tang, G., Ji, D., Hu, B., Liu, Z., Li, W., Wang, Z., Liu, Y.,
846 Wang, Y., and Ge, M.: Different HONO sources for three layer at the urban area of Beijing, Environ. Sci. Technol.,
847 54, 12870-12880, doi:10.1021/acs.est.0c02146, 2020.
848 [127] Fang, X., Li, T., Ban, C., Wu, Z., Li, J., Li, F., Cen, Y., and Tian, B.: A mobile differential absorption lidar for
849 simultaneous observations of tropospheric and stratospheric ozone over Tibet, Opt. Express, 27(4), 4126-4139,
850 doi:10.1364/OE.27.004126, 2019.
851 [128] Yu, J., Meng, L., Chen, Y., Zhang, H., and Liu, J.: Ozone profiles, precursors, and vertical distribution in urban
852 Lhasa, Tibetan Plateau, Remote Sens., 14(11), doi:10.3390/rs14112533, 2022.
853 [129] Zhang, J., Xia, X., and Wu, X.: First in situ UV profile across the UTLS accompanied by ozone measurement
854 over the Tibetan Plateau, J. Environ. Sci., 98, 71-76, doi:10.1016/j.jes.2020.05.020.
855